UC Riverside
UC Riverside Electronic Theses and Dissertations

Title

Investigating van der Waals Magnetism With Scanning Probe Techniques

Permalink

Author

Francisco, Brian Anthony

Publication Date

2024

Peer reviewed|Thesis/dissertation

UNIVERSITY OF CALIFORNIA
RIVERSIDE

Investigating van der Waals Magnetism With Scanning Probe Techniques

A Dissertation submitted in partial satisfaction
of the requirements for the degree of

Doctor of Philosophy

in

Physics

by

Brian Anthony Francisco

March 2024

Dissertation Committee:

    Dr. Yongtao Cui, Chairperson
    Dr. Nathaniel Gabor
    Dr. Jing Shi

The Dissertation of Brian Anthony Francisco is approved:

_____

_____

_____
Committee Chairperson

University of California, Riverside

Acknowledgments

I need to thank my advisor, Professor Yongtao Cui, whose journey at UCR shares a few parallels with mine; he was hired shortly before I arrived, and he had his first child shortly before I had mine. I arrived at UCR with a lot of luck following me, because I ended up under the tutelage of a researcher who is just as patient as he is insightful. Thank you for all the advice and encouragement.

My lab has grown over the many years I've been here, but I would like to bring attention in particular to labmates, visiting students and colleagues from other labs who provided me with so much help over the years, particularly Mina Rashetnia, Ben Niu, Mohammed Alghamdi, and Yingying Wu. They might not know it, but there were a lot of times when I was lost and got put on track by these people.

My wife, Nichole and my son, Jason are two bright spots on any dark day. Thank you for just being there at home for me, just being around me and supporting me. Thank you for putting up with me when grad school hit hard.

I can't have my acknowledgements take up half my dissertation, otherwise I would have a tailored message for each and every wonderful friend I've made since coming to UCR and each one I left behind by coming here. I miss each and every one of you I've said goodbye to. Thank you for giving me spaces to exist in where I wasn't a grad student for a few moments. Thank you for the games, the laughs, the conversations.

Finally, I thank my family. My mother, my sister, my in-laws, all of them. I can't imagine a more encouraging and inspiring group of people. You make feel as proud about myself as I do about all of you.

For my father, Dr. Manuel Francisco and my son, Jason. They never got to meet

each other, but they both make me who I am and who I continue to be.

For my wife, Nichole, who put up with a lot for this to happen.

For my family and friends, who probably have no idea how much they helped me.

ABSTRACT OF THE DISSERTATION

Investigating van der Waals Magnetism With Scanning Probe Techniques

by

Brian Anthony Francisco

Doctor of Philosophy, Graduate Program in Physics
University of California, Riverside, March 2024
Dr. Yongtao Cui, Chairperson

Since the discovery of graphene in 2004 a host of materials has been growing in the 2D limit including semiconductors, superconductors, and topological insulators, all of which exhibit a range of unique properties. These crystals are defined by consisting of few-atom-thick sheets which can be stacked upon one another into a myriad of combinations of heterostructures with atomically sharp interfaces that effectively become fundamentally new quantum materials. But it wasn't until 2017 that long-range magnetic ordering was observed in such systems. Bringing magnetism to the 2D regime similarly opens many doors. For example, magnetic anisotropy introduces novel interactions, and topological phenomena are more easily observed.

In this thesis, I present experiments on magnetic van der Waals (vdW) materials that share similar properties such as perpendicular magnetic anisotropy (PMA) and the presence of topological spin textures. My main method of probing these phenomena is a scanning probe technique known as magnetic force microscopy (MFM), a 2D imaging technique which is sensitive to the stray fields of the spins within a magnetic sample. I

also employ a relatively new approach to probe the interlayer exchange coupling of such magnetism using a quartz tuning fork (QTF) as a strong oscillator rotated within an external magnetic field to perform Differential Torque measurements. The results show incredible promise for a family of materials that can exhibit similar behaviors with their own unique flavors under varying circumstances.

As the synthesis of vdW magnets becomes more routine, the techniques utilized in these studies help to establish a workflow for characterizing and probing the many unrealized magnetic materials on the horizon. Additionally, the skyrmions observed in Fe_3GeTe_2 pave the way for spintronic techniques and applications. Finally, the topological magnetic textures imaged from Fe-doped TaS_2 provide insight and additional contribution to a relatively young and every growing body of knowledge in the facet of magnetically doped transition metal dichalcogenide (TMD) systems.

Contents

List of Figures

Chapter 1

Introduction

Many everyday tools and machines utilize magnetism in some way. Conventional hard drives use magnetism to store information and credit cards are read via a magnetic strip. The brush motor in a generator, the wire-bound pickups of an electric guitar, the step motors of a 3D printer, sensors in your phone and the joysticks on a video game controller all use magnetism to perform their tasks.

As one investigates further into the origin of the phenomena within these mechanisms, they find they is governed by the spontaneous alignment of electron spins within the materials, a mechanism that cannot be understood by classical physics alone. Probing these magnetic materials offers us an opportunity to gain a deeper understanding of the dynamics and interactions of these spins. My graduate work focused on the investigation of magnetism in the nigh atomically thin layered two-dimensional (2D) van der Waals crystals. I will introduce the broad family of van der Waals materials in the coming sections, with a focus on its magnetic candidates. Chapter 2 will discuss the materials pertinent to this

dissertation, Fe_3GeTe_2 (FGT) and Fe-doped TaS_2. Chapter 3 outlines different techniques used to study magnetism in this 2-dimensional limit. Chapter 4 then details my experiments probing magnetic order in the van der Waals magnets. Chapter 6 discusses new findings and insights since my measurements were performed, shining new light on the data and nigh begging for further investigation. And finally, Chapter 7 will conclude the thesis with specific issues and opportunities presented from my research.

1.1 van der Waals Materials

In most 3D crystals we are used to seeing strong ionic and covalent bonds holding the atoms of the material together within the structure. In a van der Waals material, these bonds are present within a plane defined by two axes within the crystal (usually labeled the a-b plane), whereas the bond along the third axis (typically denoted as the c-axis) is maintained by the substantially weaker van der Waals force. The disparity in bonding strength along the a-b plane and that along the c-axis allows us to easily peel layers of the material from one another, keeping the crystal periodicity of this sheet (the a-b plane) in tact, Fig 1.1 shows an example of two layers of a van der Waals material, hexagonal Boron-Nitride (hBN). By far, the most well-known example of these is graphene, which gained notoriety in 2004 when researchers first isolated it using a method known as exfoliation to separate the layers [1, 2], which ultimately lead to the 2010 Nobel Prize in Physics.

Aside from graphene, there have been thousands of other van der Waals materials that have either been discovered, experimented upon, or predicted [3]. These materials cover a wide range of beneficial applications and categories, including metals, semiconductors,
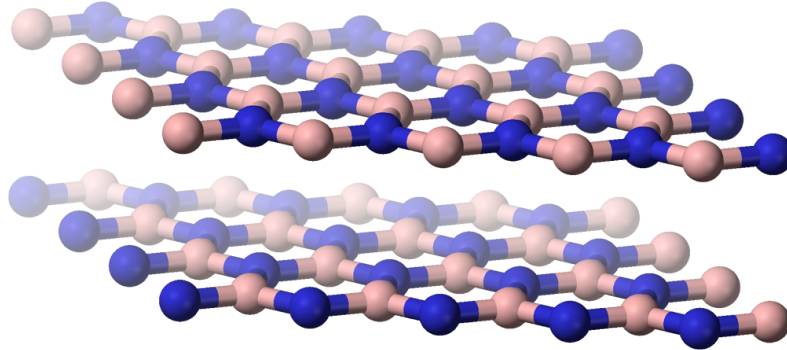
Figure 1.1: Two Layers of Hexagonal Boron-Nitride.

insulators, semimetals, superconductors, topological insulators, and magnets. Investigations from the late 2010s have revealed exotic materials presenting quantum phases with relatively accessible tunability within a single device [4, 5]. Notably, reducing the interactions to the 2D space alters the band structure [6], crystal structure [7] and phase transitions [8] from what is seen in the bulk of the same materials, revealing unique and new physical properties. While in this few layer limit, the devices and materials can also exhibit a layer dependence to these properties. As an example, a single layer graphene is a semimetal with a linear dispersion at the Fermi level [1, 2]. Conversely, bilayer graphene is a semimetal with a quadratic dispersion at the Fermi level and can have a tunable band gap controlled by a vertical electric displacement field [9].

1.1.1 Advantages of 2D Materials

2D materials offer a range of appealing characteristics that confer distinct advantages compared to both their 3D crystalline counterparts and thin films generated through bottom-up synthesis methods.

For one, the ability to transfer few-layer crystals atop one another offers the potential to create a multitude of novel synthetic compounds, referred to as van der Waals heterostructures, see Fig 1.2. Being only a few atoms thick, these crystals exhibit high sensitivity to their local environment resulting in proximity effects that can lead to the alteration of a few-layer crystal upon direct atomic contact with another substance. For instance, studies have unveiled proximity-induced spin-orbit coupling (SOC) in graphene on WS_2 [10, 11], the anomalous Hall effect (AHE) and the Zeeman spin Hall effect (ZSHE) in graphene on thin films of the magnetic insulators yttrium iron garnet (YIG) and EuS [12, 13], and valley splitting by induced magnetic field on WSe_2 on CrI_3 [14].

Secondly, in contrast to bulk crystals, 2D materials display a heightened susceptibility to gate voltages, which can be harnessed to tailor their characteristics. Consider the example of constructing a parallel-plate capacitor. Employing the 2D insulator hexagonal boron nitride (hBN) as a gate dielectric and either graphene or a metallic thin film as the opposing electrode we can independently adjust the carrier density n of the flake and apply a displacement electric field $\vec{D}_\perp$. Here we have achieved real-time control over the device's Fermi level, band structure, and their dependent properties. As a comparison, adjusting the doping level of a bulk crystal would require we substitute elements throughout the entirety of the crystal lattice (as seen with high-T_c cuprate superconductors). For bulk crystals,

every doping level requires a new single crystal to be grown with the desired properties, rather than our *in situ* gate voltage adjustment method described above.

We also see that van der Waals materials exhibit an ambivalence for substrate choice in most situations. For comparison epitaxially grown films, which possess many of the same properties we seek to explore with van der Waals materials, must adhere to whichever lattice they are deposited to. This greatly limits the substrate choice in most cases, which may make it difficult to match the requirements of the particular experiment being proposed. These thin films can also form covalent bonds with the substrate, altering the properties of the thin film itself which may not be desirable in some cases. Van der Walls materials grant the opportunity of substrate choice to suit the needs of the experiment, rather than restricting the choice to avoid undesirable effects to the sample.

As a final example of their advantages, van der Waals structures which are formed by stacking layers offer a new degree of freedom in the relative lattice orientation between layers, we call this the twist degree of freedom. Stacking layers with a misalignment due to one layer "twisted" with respect to the other forms a moiré superlattice which introduces a new electrostatic potential that has the same periodicity as the moiré unit cell, which can be on the order of tens of nanometers. Compare this to the lattice spacing of graphene which is in the low hundreds of picometers. A larger periodicity in the potential shrinks the Brillouin zone, potentially renormalizing the band structure of the sample. We saw this phenomena reveal some rich physics when graphene was placed on boron nitride [15, 16]. And in twisted bilayer graphene we've seen the aptly named magic angle of 1.1° unveil superconductivity [17] and correlated insulator states [18], opening more doors in the
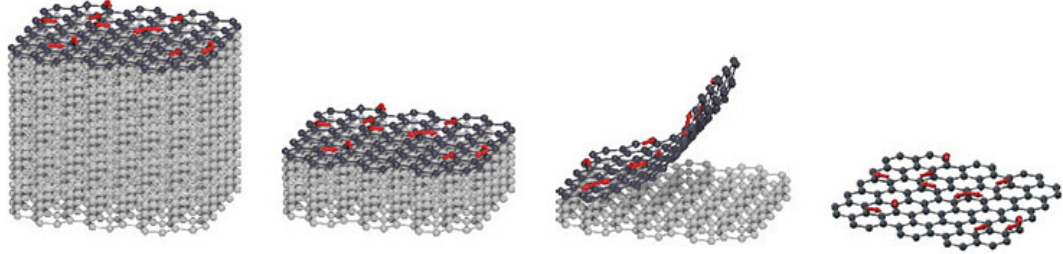
Figure 1.2: Exfoliation of van der Waals Materials. Van der Waals layers may be exfoliated and layered with other such materials. (From Flexy, Flat and Functional Magnets by Park, J.G. https://phys.org/news/2018-10-flexy-flat-functional-magnets.html)

realm of tunable moiré physics [19, 20]. Anticipated strides in experimental methodologies and theoretical comprehension of these systems are poised to unfurl a tapestry of novel revelations for the community of condensed matter physics in the forthcoming years.

1.1.2 Fabrication of van der Waals Devices

Because the van der Waals forces providing the interlayer force to hold together individual sheets of van der Waals crystals is much weaker when compared to the intralayer coupling of the sheets, we can easily isolate these sheets by way of mechanical exfoliation. This is quite a technical and fancy sounding name for such a simple process as it begins by placing bulk 3D crystal onto a piece of adhesive tape, usually the same tape used for gift wrapping. With a second piece of tape placed on top, or even folding this same tape over onto itself, layers will be cleaved from the bulk as the new tape face is removed. This process can be repeated several times to repeatedly remove layer after layer. When the

desired thickness or amount is on the tape it can be pressed onto a substrate (Si coated with SiO_2 is the typical choise) and slowly removed. This deposits some of the layers present on the tape to the substrate, resulting in varying shapes and thicknesses of crystal that usually measure tens of microns in visible top-down area and are typically below 100 nm in thickness measured normal to the substrate surface. Thickness of each piece can be determined through optical microscopy, comparing the optical contrast between pieces [21].

After identifying the desired layers, they can be stacked into a heterostructure device by employing one of many van der Waals assembly processes. A common method is the dry-transfer [22] which involves a poly(bisphenol A carbonate) or PC film is stretched over a block of polydimethylsiloxane (PDMS) mounted on a standard glass slide. With the application of a moderate amount of heat, the first flake can be picked up from the substrate and onto the PC film. Since PC and PDMS are transparent, an optical microscope can assist the fabricator in positioning the first flake with the next flake onto a second substrate by use of micropositioners. The van der Waals forces between two flat 2D crystal layers are stronger than the interactions between the crystal and the substrate, so this second flake may be easily removed again with the application of mild heating. Once all layers are assembled as desired, one need only stack them to the final substrate and remove the PC. PC will melt at 160-170º C, and any remaining residue can be removed via soaking with chloroform.

This process and the others employed by many labs are pivotal to the field when it comes to creating new heterostructure devices that combine different layered materials in unique assemblies. Another trick picked up in this field is to exploit the relatively inert

and insulating hexagonal boron nitride (hBN). With its large band gap and aversion to interactivity, hBN has become the go-to material to screen charges from the underlying SiO_2/Si substrate in such devices [23]. because SiO_2 can introduce charge inhomogeneities through its rough atomic surface and dangling bonds, this makes hBN just as pivotal as the overall assembly process. It is also most often employed as a capping layer to protect air-sensitive samples from degradation due to oxygen and moisture exposure.

1.2   van der Waals Magnets

For much of the rise of cleavable 2D materials, long-range magnetic order within few layer materials was noticeably absent from the growing list of unique and intriguing properties discovered. There was a clear interest to introduce this phenomenon to achieve long-standing goals for fundamental physics, such as the quantum anomalous Hall effect (QAHE) [24], as well as those for applications including low-power spintronics devices and topological quantum computing [25].

The Mermin-Wagner theorem [26] states that at extremely low but finite temperatures, spin-wave fluctuations prohibit long-range magnetic order in two dimensions unless there is a form magnetic anisotropy introduced. This would convince many that the idea of magnetism in a 2D regime was a mere pipe dream. However, magnetocrystalline anisotropy and spin-orbit coupling are able to stablize the magnetic ordering at low finite temperatures.

From the early 2000s to the early 2010s, while many previously studied bulk materials were being re-evalutated in the light of the 2D boom, some new two-dimensional materials were being synthesized via chemical stoichiometry. One such material is Fe_3GeTe_2,

better known as FGT. It was originally obtained from a series of experiments aimed at the syntheses of new mixed-valence compounds with transition metals related to those compounds with main group elements [27]. In 2022, we published work from our magnetic force microscopy experiments on the heterostructure of metallic FGT and insulating $Cr_2Ge_2Te_6$ (CGT) where we were able to directly image a periodic skyrmionic structure corresponding to a Topological Hall transport signal (see Chapter 4). Combined with earlier work exhibiting the high efficiency of FGT magnetization switching via spin-orbit torques [28], the spin and spin-texture related works on FGT have solidified its place and that of van der Waals magnets in general as promising options in the pursuit of consumer level spintronic devices.

Several van der Waals magnets have been proposed, validated, and investigated in the monolayer, few layer and bulk regimes. I intend to provide an overview of some of these examined magnetic materials. While the repertoire of materials within this category continues to expand steadily, there are more comprehensive reviews of 2D magnets to be found in existing literature [29].

My graduate studies were focused primarily on van der Waals materials with magnetic moments provided by iron (Fe), whether by stoichiometric synthesis (FGT) or Fe-doping (Fe_xTaS_2). Both exhibit strong perpendicular magnetic anisotropy (PMA) and strong in-plane ferromagnetic coupling. FGT and Fe_xTaS_2 also both exhibit ferromagnet ordering between their vdW planes [30, 31, 32, 33].

It is of interesting note that the iron-based magnetic materials in this dissertation exhibit metallic resistivity [30, 32, 34]. As one might expect, there are magnetic van der Waals materials which are classified as insulators and semiconductors as well, one featured

9

Material	Coupling	T_C/T_N (K)	Resistivity Regime
$Cr_2Ge_2Te_6$	Ferromagnet	60 [38]	Insulator
Fe_3GeTe_2	Ferromagnet	220 [39]	Metal
CrI_3	Ferromagnet*1 [35]	45 [32]	Insulator
$CrCl_3$	Antiferromagnet	17 [40]	Insulator
$MnBi_2Te_4$*2	Antiferromagnet	25 [41]	Topological Insulator

Table 1.1: A summary of magnetic van der Waals materials and their properties. *1, CrI_3 has been shown to possess a layered antiferromagnetic state in few layer samples at the surface. *2, The $MnBi_{2+2n}Te_{4+3n}$ family of materials are all topological insulators with different values of T_N.

in Chapter 4 is $Cr_2Ge_2Te_6$ (CGT) [8], an out-of-plane ferromagnetic semiconductor. In addition to the ferromagnetic metals and insulators, an entire realm of antiferromagnetic coupled materials have been discovered and investigated. Such materials include insulating CrI_3, which was orinally labeled a ferromagnet but has been shown to possess a layered anti-ferromagnetic state at its surface in many layered samples [35]. Insulating antiferromagnet $CrCl_3$ has been investigated in (anti-)ferromagnetic resonance setups [36], and antiferro-magnetic family $MnBi_{2+2n}Te_{3+4n}$ have garnered interest as magnetic topological insulators with an effective way of tuning interlayer exchange [37]. As mentioned, the realm of 2D magnets is vast and would be a tiresome task to comprehensively relay here. Table 1.1 summarizes the properties of several common and actively researched magnetic van der Waals materials.

1.3 Skyrmions and Topology

As the bulk of the results discussed later in this thesis will refer to topological textures known as skyrmions, it will be important to establish a foundation of knowledge on these domain structures. Topology and skyrmions are rooted in advanced fields of
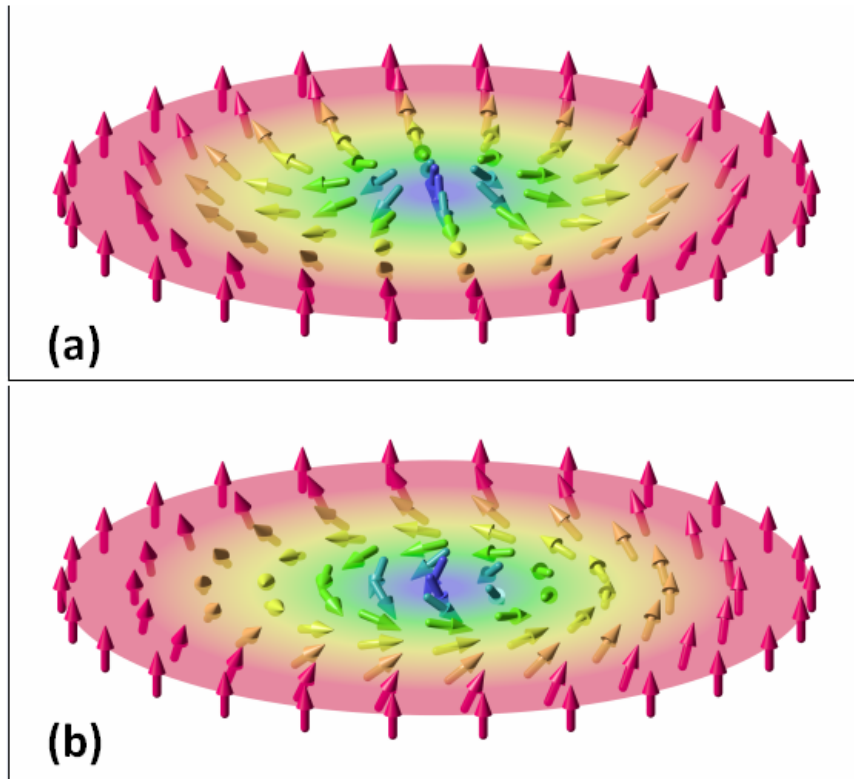
Figure 1.3: Visual representation of spins in magnetic skyrmions. a, Néel-type skyrmion and b, Bloch-type skyrmion. (Adapted with permission from Karin Everschor-Sitte and Matthias Sitte (https://commons.wikimedia.org/wiki/File:2skyrmions.PNG), 2skyrmions, https://creativecommons.org/licenses/by-sa/3.0/legalcode)

mathematics and particle theory but have much narrower scopes in the realm of condensed physics and specifically 2D magnetic systems, my aim within this section is to provide the necessary background of these topics in that particular context.

Magnetic skyrmions are topologically stable nanoscale spin textures which were first theoretically predicted by Tony Skyrme in the context of particle physics in the 1960s, but their discovery in condensed matter systems did not occur until much later [42, 43].

Skyrmions typically appear in magnetic materials with broken inversion symmetry and strong spin-orbit coupling and are often facilitated and stabilized by the Dzyaloshinskii-Moriya interaction [44, 45, 46, 47]. They are characterized by a swirling arrangement of magnetic moments, forming localized, vortex-like structures as pictured in Fig 1.3. The way in which this vortex is formed categorizes the skyrmion into one of two types: The spins that make up Néel-type skyrmions rotate 180º from center with their rotation occurring in the plane parallel to the radial direction, while those of the Bloch-type skyrmion do so in the plane perpendicular to the radial direction. They possess a nontrivial topological charge which results in skyrmions being highly stable and resistant to external perturbations, making them promising candidates for information storage and processing in spintronic devices [48]. Moreover, skyrmions can be manipulated and moved with remarkably low energy input [49, 50, 51], which holds promise for ultra-low-power computing applications.

Their are ongoing efforts toward investigating various aspects of magnetic skyrmions, including their formation mechanisms, stability, dynamics, and interactions with external fields. Research in the past decade has sought to and succeeded in creating and controlling skyrmions at room temperature in cobalt multilayers [52], and more recent efforts have seen similar success in their formation and manipulation in the room temperature van der Waals ferromagnet Fe_3GaTe_2 [53].

Chapter 2

Fe-based vdW Magnets

In this chapter, I will focus on the van der Waals materials I have primarily studied over the course of my PhD in which the magnetic moment for the material is provided in some way by the introduction of iron atoms. In the following sections, I will detail the various properties of the bulk materials, chapter 4 will detail the specifics of magnetic ordering in the few-layer limit where applicable

2.1 Fe_3GeTe_2

Iron-Germanium-Telluride, Fe_3GeTe_2, or simply FGT is an intrinsically magnetic 2D material. Meaning that it is a stoichiometrically attainable single crystal that naturally possesses ions which contribute a net magnetic moment. FGT boasts a relatively high Curie temperature (the temperature below which it transitions from paramagnet to a ferromagnet) at around 230 K for bulk samples, as well as the useful trait of being metallic when many earlier discovered intrinsic van der Waals magnets were insulators. Its high transition
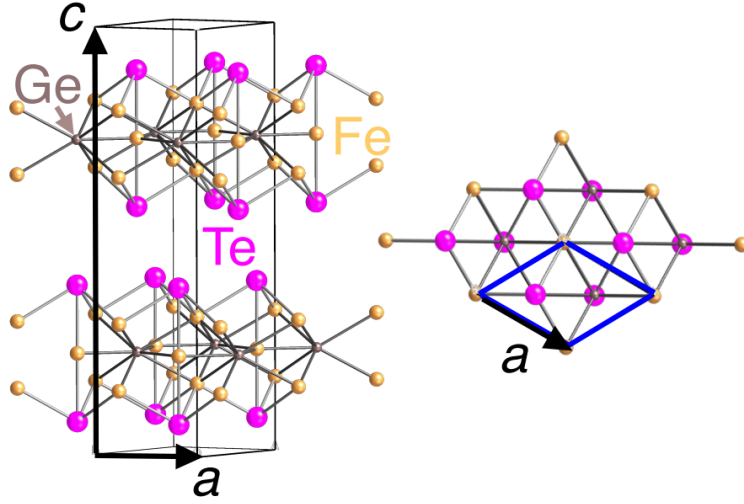
Figure 2.1: The crystal structure of Fe_3GeTe_2 (From A Van der Waals Interface Hosting Two Groups of Magnetic Skyrmions by Wu, Y., et. al. Used and edited with author permission).

temperature makes it a promising candidate for many applications and makes for slightly easier experimental parameters in some cases. Its metallic nature allows us to very easily read its magnetic state directly through Hall measurements.

As a van der Waals material, FGT is ordered in layers. Each layer consists of 5 sublayers, the top and bottom of which consist of tellurium with the remaining three hosting the iron atoms, the central layer containing germanium along with the iron as showin in Fig 2.1. This quintuple sublayer structure makes up what we refer to as a monolayer of FGT. In order to preserve the 2D long-range ferromagnetic ordering supplied by the iron atoms and their associated exchange interaction, magnetocrystalline anisotropy must exist to break through the Mermin-Wagner limit, as the Mermin-Wagner theorem precludes long-range magnetic ordering in the one- and two-dimensional limit of an isotropic magnetic system [26]. The perpendicular magnetic anisotropy is relatively strong with an anisotropy

energy of $\sim 10^7$ erg/cm^3. In varying thicknesses of FGT, electrical transport [31], magnetic force microscopy [32], and scanning tunneling microscopy [54] are all useful techniques for investigating magnetic phases in the system.

As I mentioned earlier FGT boasts metallic resistivity, allowing us to investigate much of its spin and charge features via magnetotransport. Such investigations have brought to light a large anomalous Hall current resulting from topological nodal lines [55]. Researchers have also seen the itinerant ferromagnetic ordering in FGT persisting in monolayer form, retaining the out-of-plane magnetocrystlaline anisotropy and were able to raise the Curie temperature of four-layer FGT to room temperature by way of ionic liquid gating [31]. In a five layer FGT structure, researchers witnessed a transformation from 3D to 2D Ising ferromagnetism accompanied by a rapid decrease in Curie temperature from 207 K to 130 K. Interestingly, we see that as the FGT thickness exceeds 15 nm or so the typical magnetoresistance curve lacks a square hysteresis which we now know is due to the formation of labyrtinthine domains. The ability to directly measure Hall resistivity in an FGT sample allows us to link secondary measurements directly to a magnetic state visible in the resistance curve.
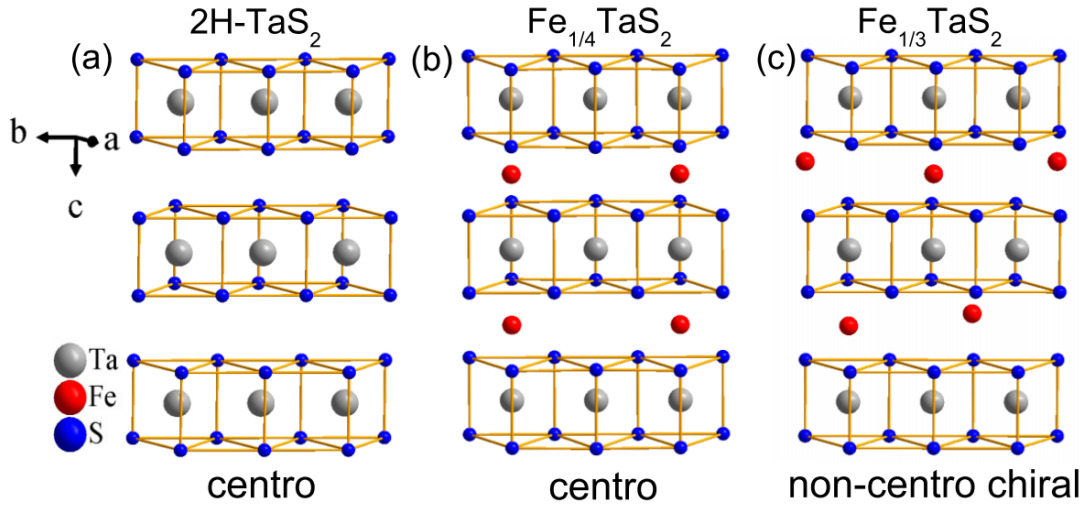
Figure 2.2: The crystal structure of Fe-doped TaS_2. a, TaS_2 in its 2H phase. b, Fe introduced into TaS_2 van der Waals gaps at a concentration of 1/4. c, Fe in TaS_2 with concentration 1/3. (From Electronic chirality in the metallic ferromagnet $Fe_{1/3}TaS_2$ by Fan, S., et. al. DOI: 10.1103/PhysRevB.96.205119)

2.2   Fe-doped TaS_2

Tantalum disulfide (TaS_2) is a van der Waals material which falls in the particular subcategory of transition metal dichalcogenide which, as the name suggests consists of a transition metal bonded to two atoms of a chalcogen element. Tantalum disulfide has three common polymorphs 1T-TaS2, 2H-TaS2, and 3R-TaS2, representing trigonal, hexagonal, and rhombohedral symmetries respectively. The 1T and 2H phases both exhibit superconductivity and charge-density wave states.[56]

It has been shown that in both its 2H and 1T phases TaS_2 can have its superconducting critical temperature increased [57] by way of iron (Fe) doping. In the early 2010s researchers investigated the effects of intercalating iron atoms into the 1T phase TaS_2 and the interplay between its charge density wave (CDW) phase and its superconductivity

16

[58]. More recently we have seen that Fe-doping the 2H phase of TaS_2 can introduce what appears to be a topological hall effect (THE) contribution to the magnetoresistance curve, demonstrating a strong transport evidence of sizable DMI and the emergence of Bloch-type spin textures such as skyrmions or chiral domain walls. When considering the system's symmetry, the doping level of Fe is of particular import as the Fe-concentration can either maintain or break the spatial inversion symmetry of the naturally symmetric TaS_2 [59].

Chapter 3

Probing van der Waals Magnetism

The introduction of ultrathin van der Waals magnets has spurred investigation into new methods to study magnetism in these crystals just a few atoms thick. Fortunately, many of the techniques originally employed for thin magnetic films were able to be adapted for van der Waals magnets over the past several years. Here I highlight two of these techniques, both of which shall be discussed in detail in their respective later chapters

3.1 Magnetic Force Microscopy

3.1.1 Fundamentals

Magnetic force microscopy (MFM) is an imaging method derived from the same principles and hardware of atomic force microscopy (AFM). In this technique, a finely pointed magnetic probe traverses a specimen's surface, revealing the magnetic configuration. Due to the magnetic force's extended reach compared to atomic forces, MFM frequently

employs a non-contact approach. MFM is not susceptible to surface impurities and is conducive to operation under ambient conditions.

MFM, much like AFM is performed by tracking the resonant frequency of an oscillating tip as it scans across a sample. The stray magnetic fields emanating from the spins within a sample will interact with a magnetized tip on the end of a scanning probe cantilever, shifting the resonant frequency up or down depending on the direction of the torque applied to the tip by these fields, which is in turn dependent upon the out of plane magnetization direction of the spins. This frequency shift, in effect measures a derivative of the vertical component of the force $\vec{F}$ between the scanning tip and the magnetic sample. The motion of the cantilever follows the equation of motion for a damped harmonic oscillator,

$$m\frac{d^2z}{dt^2} + \gamma\frac{dz}{dt} + k_s\Delta z = F_D(t) + F_{M_z}(z) \tag{3.1}$$

where m is the mass of the cantilever, γ is the damping coefficient of the oscillation, k_s is the stiffness or associated spring constant of the cantilever, Δz is the displacement of the cantilever from its equilibrium position (z_0), F_D is the external driving force providing the oscillation, F_{M_z} is the z-component of the force applied to the cantilever through magnetic torque from the sample. Considering only magnetic force on the cantilever, we can integrate $F_{M_z}(z)$ over the entire volume of the magnetized cantilever probe,

$$F_{M_z} = \frac{\partial}{\partial z}\int_{tip}(\vec{m}_{tip} \cdot \vec{H})\ dV \tag{3.2}$$

where $\vec{m}_{tip}$ is the magnetic moment of the tip and $\vec{H}$ is the stray field from the spins within the sample.
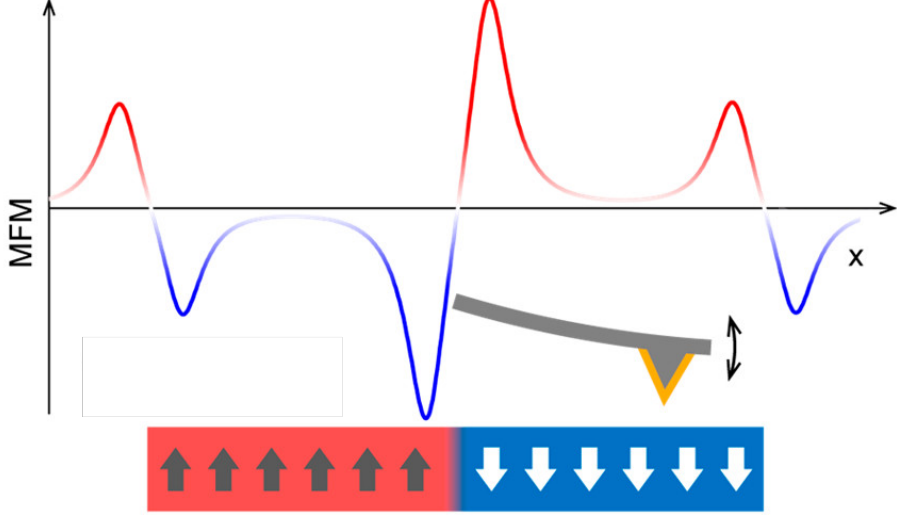
Figure 3.1: An example of a typical MFM signal line across two oppositely polarized domains. (From: Coexistence of Magnetic Orders in Two-Dimensional Magnet CrI$_3$ by Niu, B., et. al. DOI: 10.1021/acs.nanolett.9b04282. Used and edited with author permission)

When F_{M_z} is sufficiently small we may Taylor expand Eq. 3.1 to obtain,

$$m\frac{d^2z}{dt^2} + \gamma\frac{dz}{dt} + k_s\Delta z = F_D(t) + F_{M_z}(z = z_0) + \left.\frac{dF_{M_z}}{dz}\right|_{z=z_0}\Delta z \tag{3.3}$$

where can now define an effective spring constant $k_{eff} \equiv k_s - \frac{dF_{M_z}}{dz}$ and rewrite Eq. 3.1 as:

$$m\frac{d^2z}{dt^2} + \gamma\frac{dz}{dt} + k_{eff}\Delta z = F_D(t) + F_{M_z}(z = z_0) \tag{3.4}$$

The resonant frequency of this oscillator under the present conditions is given by,

$$f_0' = \frac{1}{2\pi}\sqrt{\frac{k_{eff}}{m}} \tag{3.5}$$

which can be Taylor expanded to obtain a shift, Δf from natural resonance, f_0,

$$2k\frac{\Delta f}{f_0} = \frac{\partial F_{M_z}}{\partial z} \tag{3.6}$$

where $\Delta f = f_0 - f_0'$, with f_0 being the natural resonance of the cantilever in zero magnetic field. With Δf proportional to $\frac{\partial F_{Mz}}{\partial z}$, the MFM imaging is sensitive to a change in magnetization direction as seen in Fig 3.1 and is therefore useful for imaging multidomain states.

3.1.2   Specific Instrumentation

What has been left out in the description of the MFM procedure is how to track the phase and frequency of the oscillating MFM probe. In room temperature situations, standard atomic force microscopes (AFM) can track a magnetized cantilever just as with any other probe; a laser (usually red) is deflected from the cantilever to a 4-quadrant photodetector, the deflection of the laser can be determined from the laser's location on this photodetector and the parameters of its oscillation can be calculated from it.

In our Janis VariTemp cryostat insert, many complications arise that make the room temperature AFM laser deflection setup impossible. At base temperatures (< 10 K) we can't have visible light introducing heat to the measurement area. Additionally, the 2 inch ($\sim$5 cm) diameter area which contains the sample and its probe does not offer the space necessary for deflection and an additional detector. To circumvent these issues, an interferometer is used in place of the deflection setup.

To construct the interferometer tracking for our MFM, we closely followed a procedure laid out in the PhD thesis by A. E. Pivonka [60] and adapted it to our needs. In our setup a 1550 nm laser is processed through the interferometer pictured in Fig 3.2. It first goes through a Faraday isolator (ThorLabs IO-H-1550 - Fiber Isolator) in order to
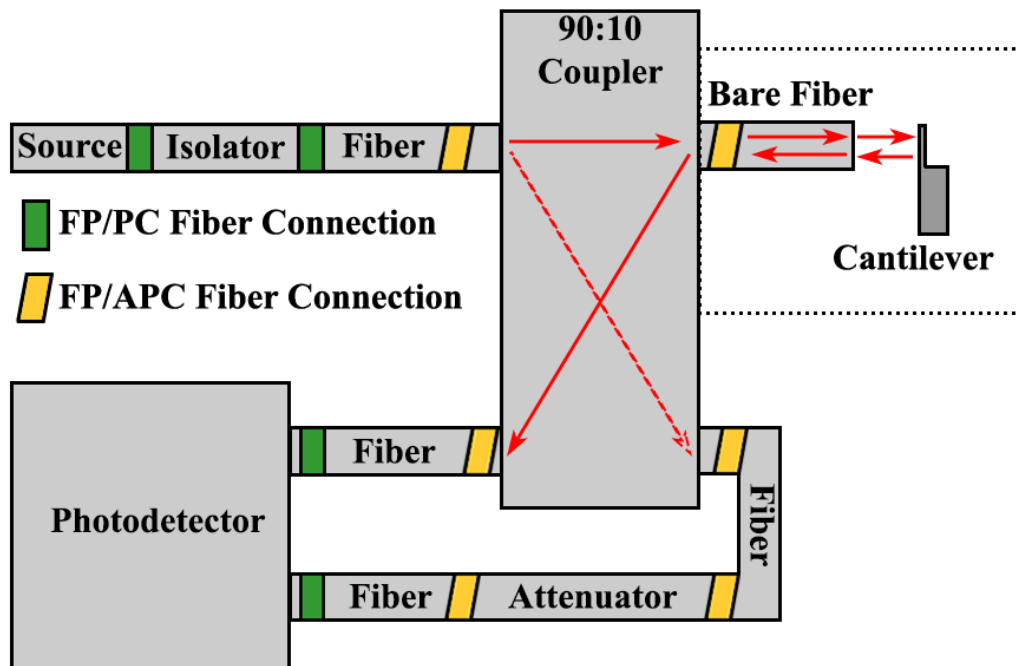
Figure 3.2: Schematic of Optical Interferometer for MFM Cantilever. The 1550 nm laser is split in a 90:10 coupler, with the smaller portion of power being directed toward the cantilever while the greater portion is routed to the photodetector as reference. The main signal to the photodetector is the interference of the two reflections within the cryostat area (dashed line box), which differ in path length by twice the distance from the bare fiber to cantilever. (Image is derivative from Nanoscale Imaging of Phase Transitions with Scanning Force Microscopy by Pivonka, A. Adapted with permissions)

avoid optical feedback into the laser source. The signal is then split via a 2x2 90:10 split coupler (TW1550R2A2 - 2x2 Wideband Fiber Optic Coupler) where 10% of the signal is fed through the cryostat to the cantilever, and the other 90% is redirected to the photodetector for reference (after attenuation through a VOA50-APC - SM Variable Attenuator), the purpose of which is to reduce noise from fluctuations in laser power output. The attenuator is adjusted to roughly match the incoming power of the main signal that reaches the other end of the photodetector. The end of the optical fiber which is fed through the cryostat and hits the cantilever probe arm itself has been cleaved for a clean normal endpoint, which will provide a point of reflection for the laser, which is again processed through the coupler, where 90% is fed to the other end of the photodetector, the other 10% is essentially lost with its reflection toward the laser source being stopped by the isolator. In the cryostat, the portion of light that is not reflected at the fiber cleave will continue and reflect off the cantilever, entering the fiber again and returning to the interferometer along with the original reflection from within the fiber. These two reflections interfere with one another en route back to the photodetector at the end of the interferometer and differ in path length by twice the distance to from fiber to cantilever. We can adjust this distance with a stack of piezoelectric material that holds the optical fiber in place (ThorLabs PK4FXH3P2 Piezoelectric Stack with Through Hole), adjusting this position via a DC voltage to a point of maximum sensitivity to changes in this signal (maximizing the derivative of the signal). With the interferometer sensitive to small changes in the cantilever-fiber distance, now the finer oscillation of the cantilever can be detected.
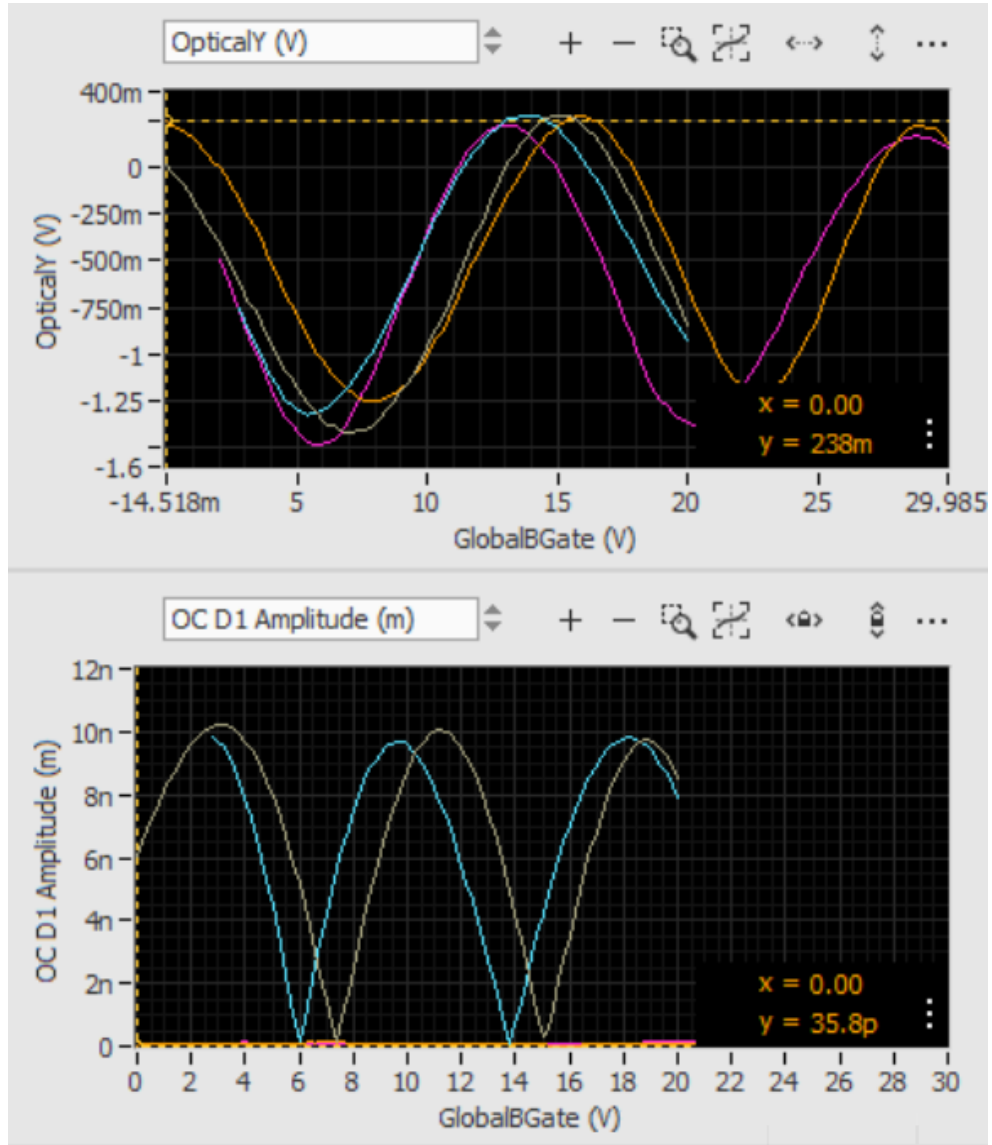
Figure 3.3: The Optical Signal Plotted Against the Applied Voltage to Piezoelectric Stack. Top: Direct readout of optical interferometer signal from photodetector, oscillating as distance between cantilever and optical fiber changes. Bottom: Oscillation amplitude measurement as a function of applied voltage, as the derivative of the top graph appraoches zero, the sensitivity to the oscillations is reduced until they cannot be detected. The maximum sensitivity is at points of maximum derivative.

As mentioned before, the distance between bare fiber and cantilever can be finely adjusted by use of a piezoeletric chip stack which holds the optical fiber. By applying a strong DC voltage (ranging 0-15V at room temperature, 0-40 V below 20K) to this piezo stack, we can have the end of the optical fiber finely approach or retract from the cantilever. We use Nanonis software and High Voltage Amplifier to apply this voltage and read both the applied voltage and the photodetector signal, as seen in Fig 3.3. The piezo stack will expand under positive voltage, approaching the fiber to the cantilever, decreasing the distance. The optical signal will oscillate between its minimum value at path length difference $\Delta\ell = (n + \frac{1}{2})\lambda$ and its maximum value at $\Delta\ell = n\lambda$. Since the path length difference is twice the distance from fiber to cantilever, $\Delta\ell = 2s$, where s is the fiber-cantilever separation, The spatial difference between these extrema corresponds to a distance of $\frac{1}{4}\lambda$. From this information we can extract the sensitivity of the optical readout, calculating a calibration factor in units of m/V. When the attenutator is adjusted such that the power of the reference signal is equal to that of the main signal's incoming power to the photodetector, the photodetector's signal, V_{photo} can be described as

$$V_{photo} = \frac{V_{pp}}{2}cos\left(\frac{4\pi s}{\lambda}\right)$$ (3.7)

Where V_{pp} is the peak-to-peak voltage of the photodetector readout, s is the fiber-cantilever separation distance, and λ is the wavelength of the laser source (1550 nm in this case).

$$\left|\frac{dV_{photo}}{ds}\right| = \frac{2\pi V_{pp}}{\lambda}\ sin\left(\frac{4\pi s}{\lambda}\right)\bigg|_{s=\frac{\lambda}{8}} = \frac{2\pi V_{pp}}{\lambda}$$ (3.8)

25

The calibration factor is taken from setting the magnitude of this derivative to it's maximum value, which from Eq 3.8 can be seen to occur at $s = \frac{\lambda}{8}$. Taking the reciprocal of this expression we have the calibration factor of $\frac{\lambda}{2\pi V_{pp}}$ m/V. At 1550 nm we can achieve a relatively desirable calibration of ~ 50nm/V with a $V_{pp} \sim 5$V.

With a laser in the infrared regime and no guarantee that 100% of the laser will avoid the sample, we wish to reduce heating effects while still maintaining a good signal strength. More systematic tests could optimize this, but we've so far had a very good signal with no heating effects at initial laser power of ~ 0.3 mW.

3.1.3 Thickness Dependence of MFM Signal

The earlier section details the fundamental theory of MFM detection; however, the MFM signal was found to be proportional to the thickness of the ferromagnetic layers that exhibit a net vertical moment when in the saturated single domain state [35]. This is shown via finite element simulation in COMSOL in Fig 3.4. In the simulation, I kept the probe at a fixed height of 150nm above the simulation sample, but increased the thickness of the sample by adding layers below and sampling the $\frac{dB_z}{dz}$ signal. Each layer is saturated magnetization, thus as the thickness increases from 0 to 1000 nm, the net magnetic moment that is probed increases. In the region we typically have our samples (< 200nm), the MFM signal is basically linear. This implies that each subsequent layer roughly contributes equally to the overall signal, contrary to intuition suggesting that the $\frac{1}{r}$ dependence of field strength would make lower layers less important. This is because when the magnetic state is uniform in a relative wide but thin magnetic flake, the magnetic field near the flake surface decays very slowly, recall that our tip-sample separation is orders of magnitude smaller than the

26
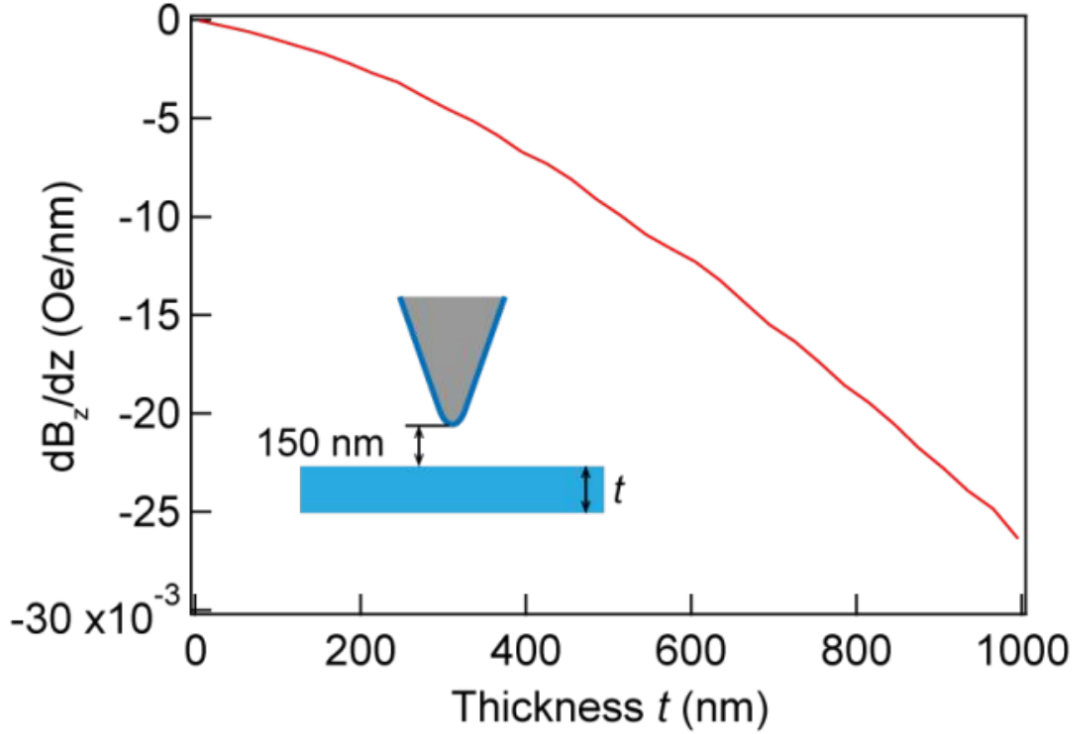
Figure 3.4: Finite Element Simulation of MFM Signal vs Sample Thickness. The derivative is evaluated at a fixed height (150 nm) from the top surface of the flake.

lateral size of our typical samples. While the field, B_z decays slowly as a function of z at these lengths, $\frac{dB_z}{dz}$ decays even more slowly. Hence, one must consider what is happening within the sample and not just the surface conditions.

3.1.4 Fourier Analysis of MFM Data

When analyzing the visual MFM data, especially when investigating topological phenomena, it may be important to discern whether or not the features appear at some discrete spatial frequency. That is, are these features regularly sized and regularly spaced apart in some measurable and predictable way? This is important because topological

27

domains will resist the effects of spatial defects and maintain particular sizes and distances from other such features as dictated by the forces that bring them about [61]. Therefore, the existence of phenomena occurring at regular spacing and sizes can be another indicator that what we are seeing is in fact topological in nature. One particularly effective and accessible way to extract the frequency of their occurrence is to take a 2D Fourier transform of the visual data. The resulting image will be a sort of heat map of frequencies present in the image, with the value in the center representing how much of the image is unique, unrepeated features.

The FFT spectra can also be used to filter images and extract a more clear view of what is being detected. Noise and other undesirable features can be masked out in the FFT spectra before performing and inverse transform to reconstruct a new MFM image. For example, random noise generally contributes to a central gaussian peak in the FFT, reducing the weight of this peak in the inverse transform will recreate the MFM image with less of the noise present in the original image. Hinging on this same concept, periodic features of interest found in the FFT may be isolated and reimaged in order to see how they show up in the MFM frame.

The 2D Fast Fourier Transform data in this dissertation was performed, masked, and filtered using the Gwyddion SPM data visualization and analysis tool, as well as the Numpy package for python.
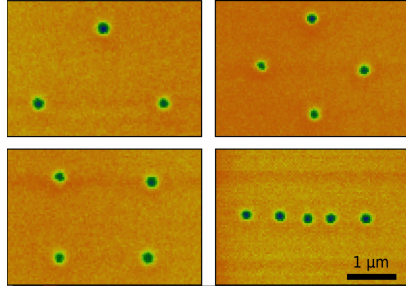
Figure 3.5: Individual skyrmions captured with MFM imaging. (From Individual skyrmion manipulation by local magnetic field gradients by Casiraghi, A., et. al. http://creativecommons.org/licenses/by/4.0/.

3.1.5 Imaging Skyrmions with MFM

Due to the MFM signal depending on the height derivative of magnetic force on the magnetic moment of the cantilever probe, a selection of out-of-plane or in-plane sensitivity must be made and increasing sensitivity to one will reduce it to the other. In most setups, including our own in this thesis, the probe is most sensitive to out-of-plane magnetization. This is ideal for magnets with perpendicular magnetic anisotropy (PMA), but could add difficulties when imaging domains with in-plane projection to their magnetization, as is the case with skyrmions. Without the assistance of additional spatial magnetic probing techniques such as Lorentz transmission electron microscopy (LTEM), it may not be possible to discern the alignment of the sections of in-plane magnetization in skyrmions through MFM alone. As such, skyrmions present as circular bubble-like features in the MFM image, with a strong polarization in the center and an oppositely aligned circumference at some radial distance determined by the skyrmion size [62]. Examples can be seen in Fig 3.5
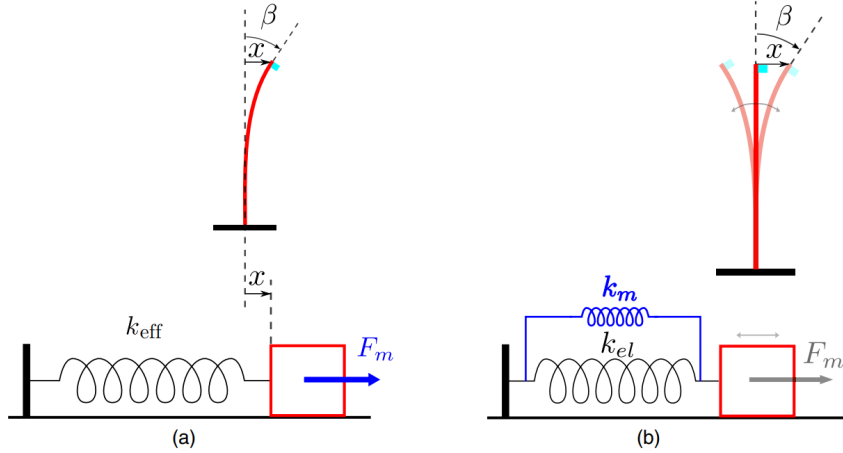
Figure 3.6: Torque Magnetometry and Torque Differential Magnetometry modeled as mass-on-spring oscillators a, standard torque magnetometry. b, torque differential magnetometry. (From: Theoretical model for torque differential magnetometry of single-domain magnets by Kamra A., et. al. DOI: 10.1103/PhysRevB.89.184406)

3.2   Torque Differential Magnetometry

An attractive method for measuring magnetic interactions in bulk materials is torque magnetometry. The measurement is relatively straight-forward; an externally applied magnetic field exerts a magnetic torque on the sample which is at the end of a mechanical oscillator. The orientation between the external field and the sample plane of choice is rotated and the torque exerted by the constant field can be recorded to map out its dependence upon relative angle. Being as torque can be expressed as the derivative of free-energy density, this data can be a tool in extracting the constants which parametrize F, such the exchange interaction strength and the anisotropy strength [63].

As with any mechanical oscillator, we can begin modeling the torque differential experimental setup as a mass on a spring as in Fig 3.6. Just as with the mass on a spring example, we can refer to the magnetic sample's displacement from equilibrium as x while expressing its resonant frequency in terms of an effective mass (m_{eff}) and spring stiffness (k_{eff}).

$$f = 2\pi \sqrt{\frac{k_{eff}}{m_{eff}}} \tag{3.9}$$

For sufficiently small displacements about the equilibrium point, the restorative force may be expressed as the sum of elastic force $F_e(x)$ with the magnetic force $F_m(x)$, which is an effective force representing the effect of the torque component of torque perpendicular to the plane of oscillation, $\tau_m^{\perp}(x)$ exerted on the magnetic sample by the external magnetic field, H_{ext}.

With the distance from the magnetic sample on the tip to the the fulcrum of oscillation being L, a Taylor expansion of $\tau_m^\perp(x)$ around equilibrium results in retorative force given by

$$F_{res} = -kx + \frac{1}{L}\frac{d\tau_m^\perp}{dx}|_{eq}x = -k_{el}x - k_m(H_{ext})x, \tag{3.10}$$

with k_{el} and k_m representing stiffness in the contexts of elasticity and magnetism respectively and are the contributors to $k_{eff} = k_{el} + k_m$. The linear derivative can be written to instead be dependent on angular displacement β where $x = L\beta$ and $dx = Ld\beta$ to obtain

$$k_m(H_{ext}) = \frac{-1}{L^2}\frac{d\tau_m^\perp}{d\beta}|_{eq} \tag{3.11}$$

When assuming $k_m << k_{el}$ we can write a frequency shift due to magnetic torque as

$$\frac{\Delta f}{f_{el}} = f_{el}\frac{\Delta k_m}{2k_{el}} = -\frac{f_{el}}{2k_{el}L^2}\frac{d\tau_m^\perp}{d\beta}|_{eq} \tag{3.12}$$

showing that the shift in resonant frequency can be considered to be directly proportional to the torque derivative [64].

3.2.1 Magnetometry with a Tuning Fork and the QPlus Mode

Quartz tuning forks (QTFs) have gained popularity in use for scanning probe microscopy because of the surprisingly high quality factor (Q factor) resulting in a low frequency variation. Aside from these uses, QTFs have the potential for high-sensitivity magnetometry for the same reasons as well as their high sensitivity [65]. In previous cantilever experiments, the readout of the magnetization signal usually involves some method to drive the mechanical oscillator and typically detection of cantilever deflection is done with some form of optics, resulting in a cumbersome setup that is sensitive to environmen-
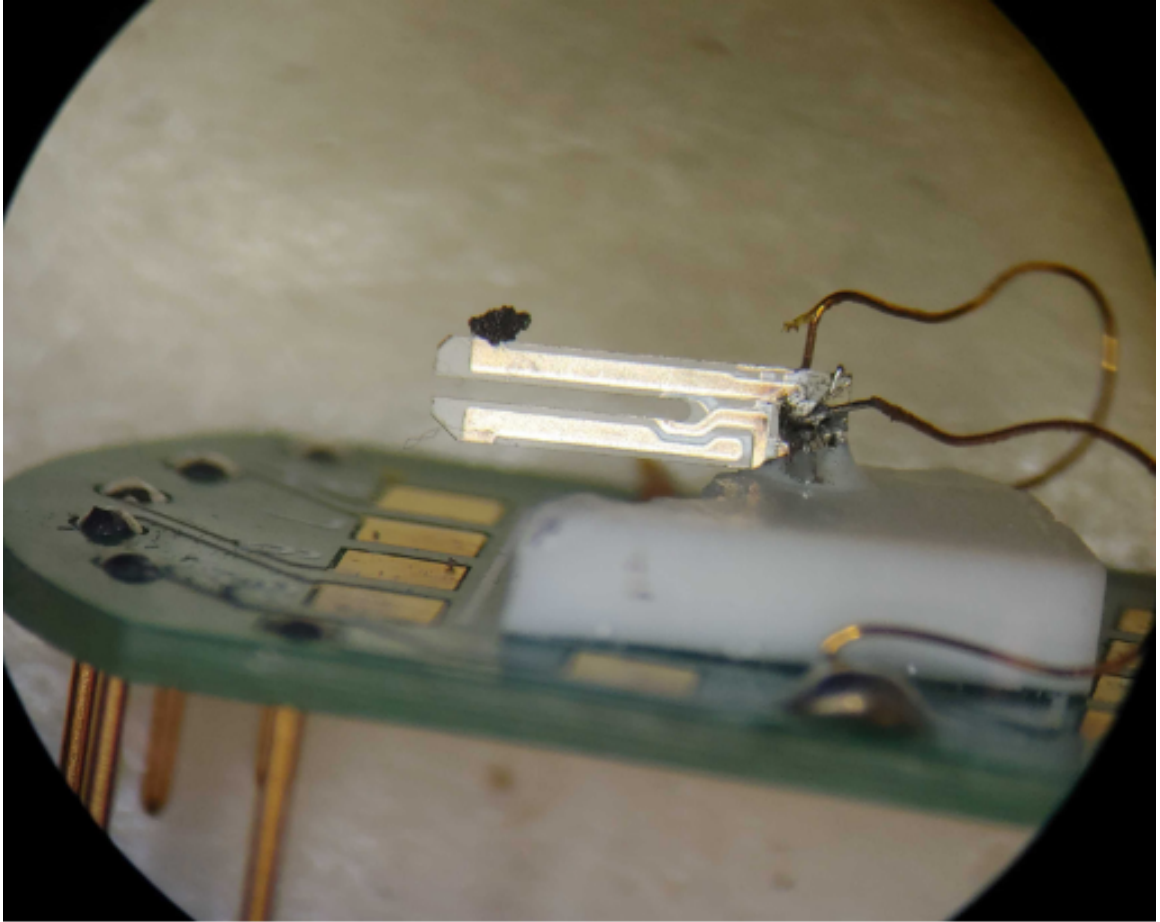
Figure 3.7: A piece of bulk Fe_3GeTe_2 attached to the end of one prong of a quartz tuning fork.

tal factors [66, 67]. As such, it would be beneficial to develop an easy-to-set-up and highly sensitive magnetometry with a QTF.

But, affixing a mass to the end of one prong of a two prong system introduces asymmetry to the QTF, greatly reducing the once high Q factor (see Fig 3.7. It has been shown that an alternate mode of use for the QTF can result in a mitigation of such an effect, by holding one prong of the QTF stationary, essentially making it an electrically driven cantilever [68]. More recent work has seen success with this single prong QTF mode
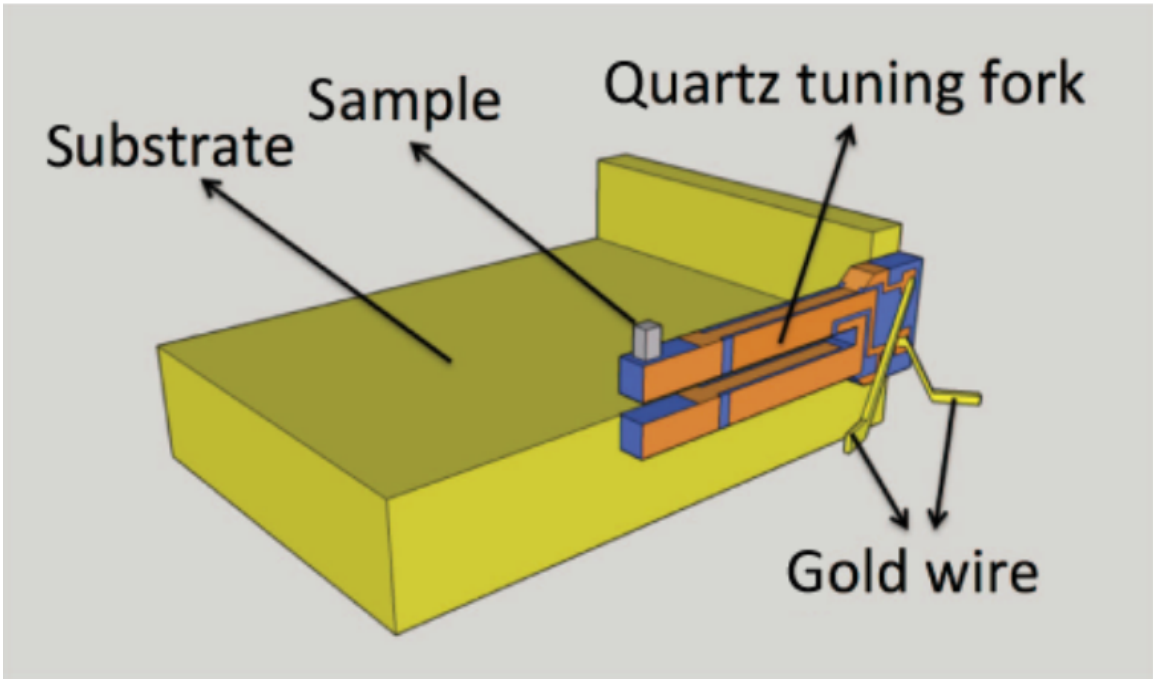
Figure 3.8: A quartz tuning fork in qPlus configuration. (From Torque Differential Magnetometry Using the qPlus Mode of a Quartz Tuning Fork by Chen, L., et. al. DOI: 10.1103/PhysRevApplied.9.024005)

(dubbed qPlus) in use for torque differential magnetometry [69]. An illustration of a QTF in qPlus mode can be seen in Fig 3.8.

The torque differential magnetometry measurements presented in this dissertation were performed in a Quantum Design Physical Property Measurement System (PPMS) with data collected through a custom interface designed in LabVIEW from National Instruments. The details of this setup can be found in Chapter 5.

Chapter 4

MFM Measurement Results

Here I detail the procedures and results of the measurements made with the magnetic force microscopy technique. Section 4.1 is adapted with permission from a previously published work I co-authored (DOI: 10.1002/adma.202110583). In the adaptation presented here I have expanded on the discussion of the data and the use of the Fourier transform in the data analysis.. Section 4.2 details a work-in-progress that I plan to draft and publish in the coming year.

4.1 Imaging Magnetic Skyrmions in Fe_3GeTe_2

4.1.1 Introduction

Two dimensional (2D) magnetism was recently discovered in van der Waals (vdW) ferromagnets [30, 31, 32] and antiferromagnets [39, 70, 71], providing unprecedented opportunities for exploring magnetism, and towards spintronic applications in the 2D limit [72, 73]. Among all the interface engineered heterostructures based on vdW layered systems,

magnetic proximity effect is integral to manipulating spintronic [74, 75, 76], superconducting [77, 78, 79] and topological [80, 81, 82] phenomena. Topological magnetic skrymions have been well studied due to their nontrivial topology, which lead to many interesting fundamental and dynamical properties [83, 61, 48]. These have been reported mostly for non-centrosymmteric single crystals [84, 43, 85], ultrathin epitaxial system [86, 87], and magnetic multilayers [88, 89, 90, 91, 92]. Recently Néel-type skyrmions were observed in a vdW ferromagnet interfaced with an oxidized layer [93] or a transition metal dichalcogenide [51] with a control of the skyrmion phase through tuning of the ferromagnet thickness. Furthermore, with a variety of vdW magnets, skrymions phase could be created in their new interfaces with unique properties.

Materials hosting multiple skyrmion phases add richness to the field, with an additional degree of freedom in designing devices. Such a degree of freedom adds value as a means to lower the error rate in racetrack memories with skyrmions as information carriers [94, 95]. Multiple skyrmion phases have been reported in FeGe grown on Si(111) at low temperatures [96] and in Ir/Fe/Co/Pt multilayers[94]. Different from these thin film systems, vdW heterostructures possess well defined and ordered atomic layer range of thicknesses, atomically sharp interfaces and easy electrical field control. Forming a heterostructure of two vdW ferromagnets allows breaking of inversion symmetry at the interface [61], with skyrmions expected inside both these two ferromagnetic layers in the context of strong spin orbit coupling. So far, there are no direct observations of the multi groups of magnetic skyrmions at a vdW interface.
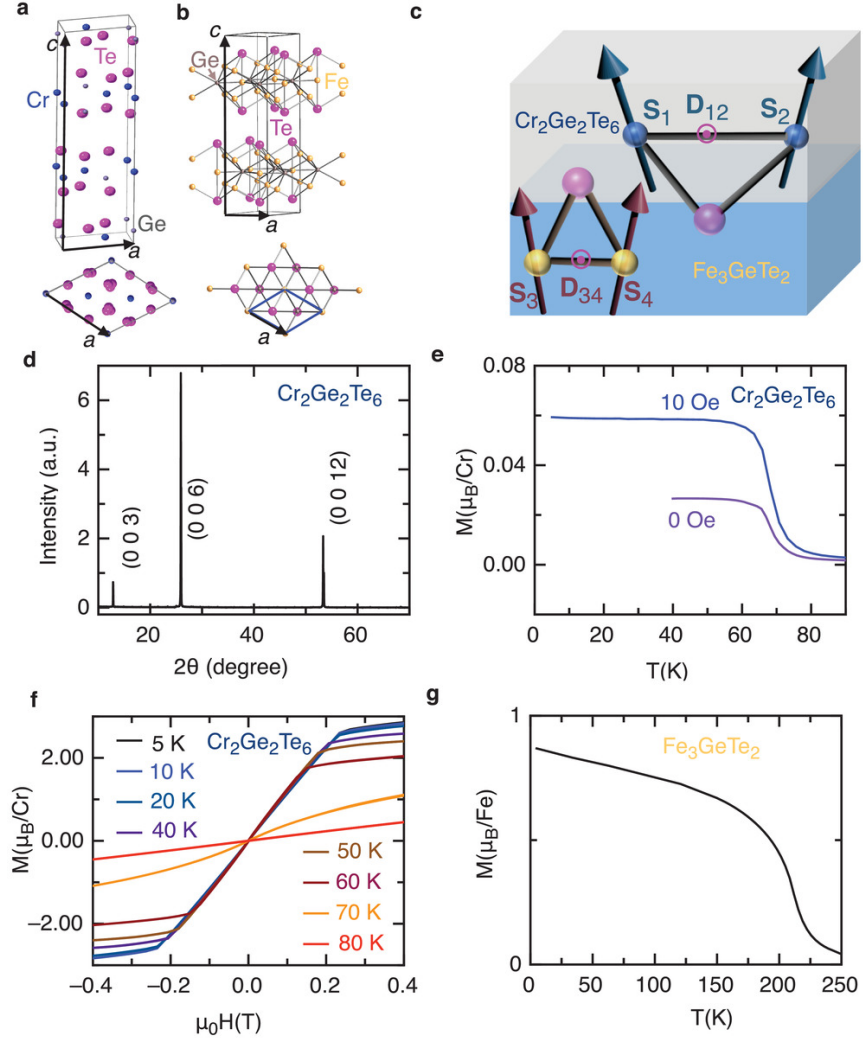
Figure 4.1: Structure and magnetic properties in FGT and CGT crystals. a, Crystal structure of CGT. b, Crystal structure of FGT. c, DMI is induced at the interface of CGT and FGT. d, X-ray diffraction pattern of CGT. e, The temperature dependent magnetization profile of CGT. f, Magnetic hysteresis of CGT with applied magnetic field H // c-axis. g, The temperature dependent magnetization profile of FGT.

In this work, we demonstrate a vdW interface, i.e. $Fe_3GeTe_2/Cr_2Ge_2Te_6$

(FGT/CGT) interface, can host two groups of magnetic skyrmions. The initial signature

for this comes from the observation of the topological Hall effect (THE). Below the Curie

temperature ($T_C \sim 65$ K) of CGT, Hall resistivity shows two sets of kinks, due to the

magnetic skyrmion phase formation on CGT and FGT sides. Above 60 K, there is only one set of kinks seen in the Hall resistivity, likely arising from the skyrmion phase on the FGT side. To ascertain and understand the origin of THE, magnetic force microscopy was used to image the skyrmion lattice directly. These observations could provide a new platform for designing a robust skyrmion-based memory and computing architectures by coding the information in multiple groups of skyrmions.

4.1.2 Ferromagnetic Fe_3GeTe_2 and $Cr_2Ge_2Te_6$ thin layers

CGT is a soft, 2D layered ferromagnetic crystal, with rhombohedral structure and vdW stacking of hexagonal layers. As illustrated in Fig. 4.1a, a layer of Cr atoms is sandwiched between two Ge-Te layers, forming a monolayer of CGT. Its lattice parameters are a = 6.826 Å and c = 20.531 Å. Among the 2D magnets, FGT is a ferromagnet with a strong perpendicular magnetic anisotropy. Bulk FGT consists of weakly bonded Fe_3Ge layers that alternate with two Te layers with a space group $P6_3mmc$ as shown in Fig. 4.1b with lattice parameters a = 3.991 Å and c = 16.333 Å [97]. For both pristine CGT and FGT crystals, the inversion symmetry is preserved inside the bulk. However, by forming an interface between these two materials, the inversion symmetry is broken. With spin-orbit coupling present, Dzyaloshinskii-Moriya interaction (DMI) is induced at the interface as shown in Fig. 4.1c, both at FGT and CGT interfacial layers. The DMI between two atomic spins $\mathbf{S_1}$ and $\mathbf{S_2}$ can be expressed as: $H_{DM} = -\mathbf{D_{12}} \cdot \mathbf{S_1} \times \mathbf{S_2}$.

The crystal structure of grown CGT crystal was analyzed by using X-ray diffraction studies as depicted in Fig. 4.1d. Typical peaks corresponding to the (003), (006) and (0012) planes in CGT were observed. These peaks indicate that the layered CGT crystal with good quality is achieved. The T_c for CGT was around 65 K, as seen from magnetization measurement using a magnetometer(Fig. 5.1e). The ferromagnetic order in CGT develops at low temperatures upon cooling down both without and with an out-of-plane magnetic field. The magnetic hysteresis is shown in Fig. 5.1f, where the ferromagnetism disappears above 65 K. Compared to CGT, FGT has a much higher T_c of around 200 K, as shown in Fig. 4.1g.

4.1.3 Two Sets of THE Signals

THE can arise from the accumulated Berry phase acquired by electrons in the adiabatic limit as they encounter a skyrmion along their path. However, recent experiments offered an alternative interpretation of the topological Hal effect reported in topological insulator heterostructures; they attribute the topological Hall signals to the overlapping of two anomalous Hall signals with opposite signs. A similar reasoning was used to explain the topological Hall-like signatures (one peak and one dip) in $SrTiO_3/SrRuO_3/SrTiO_3$ [98] heterostructures. In such a scenario, the competing anomalous Hall signals contributing to topological Hall-like signatures originate either from the coexisting surface and bulk magnetic phases in the magnetic topological insulator system [99], or two interfaces in the heterostructures. As opposed to previous systems, this current FGT/CGT bilayer system might facilitate the demonstration of THE for three reasons: (1) only one interface is formed between the two materials; (2) two sets of kinks, a signature for THE at both sides

of an interface, are observed when the temperature is lower than the T_C of CGT; and (3) skyrmions are imaged directly by magnetic force microscopy (MFM).

In the transport measurements, CGT/FGT thin films were transferred onto prepared Hall-bar bottom electrodes under a microscope inside the glove box (N_2 atmosphere), and the resistivity was measured with lock-in technique. The CGT layers for the transport measurement have a thickness between 30 nm and 40 nm, which is relatively insulating compared to metallic FGT layers. Magnetic field was applied perpendicular to the sample plane. As shown in Fig. 4.2a, 20-layer (20L) FGT exhibits square hysteresis loop when the temperature is below 200 K, demonstrating a strong perpendicular out-of-plane magnetic anisotropy. When FGT thickness was reduced to 5L, interface coupling between FGT and CGT gave rise to pronounced peaks and dips near the magnetic transition edge, the signature of THE. Different from previously reported systems, two sets of THEs (as indicated by blue and orange circles in Fig. 4.2b) are observed in this heterostructure of two ferromagnets.

The topological Hall resistivity value is related to carrier density n, and an effective field B_{eff} generated by skyrmion lattice $\left(\rho_{xy}^{THE} \sim \frac{1}{ne} B_{eff}\right)$ [100]. The different magnitude of the topological Hall resistivity value indicates two groups of skyrmions with different sizes. These two sets of THEs coexist when the temperature is below the T_C of CGT. One set indicated by the orange circles vanishes at 60 K and above, is attributable to the disappearance of ferromagnetic order in CGT with increasing temperature. It may be noted that, this THE is only observed in CGT/5L FGT sample. The absence of THE in this heterostructure with thicker FGT can be due to the high carrier density. With larger carrier
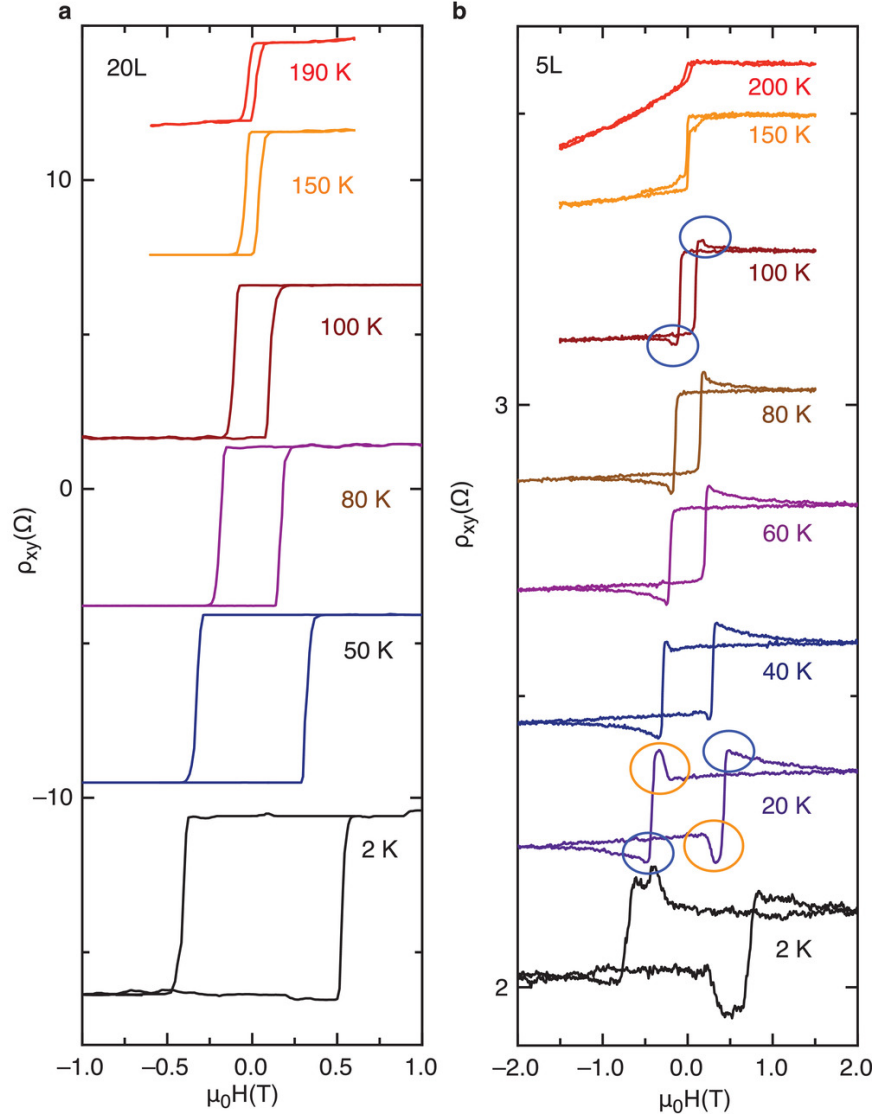
Figure 4.2: Hall resistivity (shifted for clarity) of a CGT/FGT heterostructure with different FGT thickness of a, 20L, and b, 5L. A magnetic field was applied perpendicular to the sample plane. A square hysteresis loop indicates the perpendicular magnetic anisotropy. Peaks and dips appear in heterostructure with 5L FGT, signifying the existence of topological Hall effect.

density in thicker FGT samples, the topological Hall resistivity is dwarfed in comparison. For example, for 20L FGT at 20 K, the estimated topological Hall resistivity contribution is less than 10^{-3} Ω, assuming a skyrmion lattice with a size of 100 nm. This resistivity value

41

is more than two orders of magnitude smaller than the anomalous Hall resistivity, and thus

tends to be buried in the anomalous Hall signals.
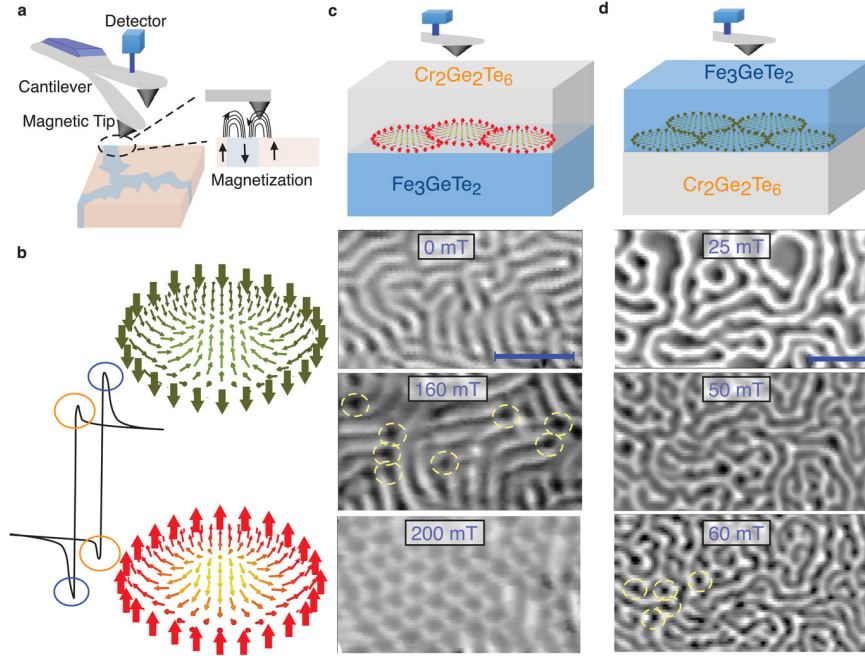
Figure 4.3: Skyrmions at both sides of $Fe_3GeTe_2/Cr_2Ge_2Te_6$ interface imaged by MFM. a, Schematic illustration of MFM measurements. b, Two sets of THE signals observed for temperatures lower than 60 K. The peak and dip features of THE resistivity indicating the skyrmions with opposite polarity. c, Skyrmion lattice observed on CGT side with a magnetic field of 200 mT and a temperature of 20 K. Scale bar: 1 µm. d, Skyrmions on FGT side start to appear with a magnetic field of 50 mT at a temperature of 100 K. Scale bar: 1 µm.

4.1.4 Directly Imaging the Skyrmions with MFM

To further examine the origin of THE arising at the FGT/CGT interface, we

performed low-temperature MFM measurements under applied magnetic fields. (resolution

of the MFM measurement can be found in Chapter 3) In MFM, the magnetic stray field

originating from nanoscale features on the surface of a sample is detected by a scanning

nanoscale magnetic tip (Fig. 4.3a). Note that in our topological Hall resistivity, two sets of kinks were observed, attributable to magnetic skyrmions on FGT side and CGT side, respectively (Fig. 4.3b). In our MFM measurement geometry, the MFM signal characterizes the second order derivative of the out-of-plane component of the stray magnetic field, i.e., $\frac{\partial^2 H_z}{\partial z^2}$. For samples with out-of plane magnetization, MFM responds both inside individual domains and at the domain walls. Fig. 4.3c shows a series of MFM images taken on CGT/FGT device (same device as in Fig. 4.2b) with applied perpendicular magnetic fields at 20 K. As the field increases from zero, the image shows a labyrinth domain feature. Upon increasing the field to 160 mT, skyrmionic features started to form as indicated by the yellow circles in Fig. 4.3c. At 200 mT, skyrmion lattice with a size of $\sim$ 130 nm was directly imaged. This skyrmion lattice disappears and the sample enters into a uniform single domain as the field is increased to 250 mT). This observed magnetic skyrmions are expected to occur at the interface close to CGT side for three reasons: (1) with CGT on top of FGT, MFM signals would be dominated by the magnetic fields generated by the CGT layer, (2) the magnetic signal from 5L FGT under multilayer CGT is too weak or screened to be observed, and (3) the formation of magnetic skyrmion lattices exactly matches the magnetic field which lead to the development of THE on CGT side (the dip at a positive magnetic field in Fig. 4.2b and 4.3b).

With a reversed sample structure, i.e., FGT on top of CGT, MFM measurements show domain images in FGT side in Fig. 4.3d. At 100 K, FGT shows similar labyrinth domain feature at 25 mT but with a larger domain width, compared to CGT case at 20 K. When the field was increasing, skyrmions started to appear, as indicated by the yellow

circles. The skyrmion size was estimated to be ~ 180 nm (100 K and 60 mT) and decreasing as the temperature went down.

The skyrmion lattice in CGT/FGT develops with the magnetic field. When sweeping from a negative field (-2 T) which is large enough to saturate CGT magnetization at 20 K, the skyrmions develop at ~ -50 mT (Fig. 4.4a). Interestingly, the magnetic skyrmions are seen to persist when the applied magnetic field is turned off, in the remanent state. Emergence of magnetic skyrmion at 0 T magnetic field has been predicted to be a possible signature of Moiré skyrmions [101]. The real reason and mechanism of zero-field magnetic skyrmions is not clear in our case at present. One should also consider the role of the exchange coupling between CGT and FGT, where FGT provides an effective field at the interface. When the magnetic field was further increased to 120 mT, skyrmion lattice emerged forming a hexagonal pattern. Further increasing the magnetic field to 140 mT, the skyrmion images switched to opposite contrast due to the flip of tip magnetization by the external magnetic field.

The skyrmion size was extracted from THE and the skyrmion images by MFM measurement (Fig. 4.4b). The skyrmion size for both FGT and CGT side decreases with decreasing temperature. The error bars for data points in the MFM measurement (dots and squares with dashed lines) are due to the variation of skyrmion size under applied magnetic field. The skyrmion size extracted from the THE (dots and squares with solid lines) offers an order of magnitude estimate, which is around one order of magnitude smaller than that from MFM measurement.
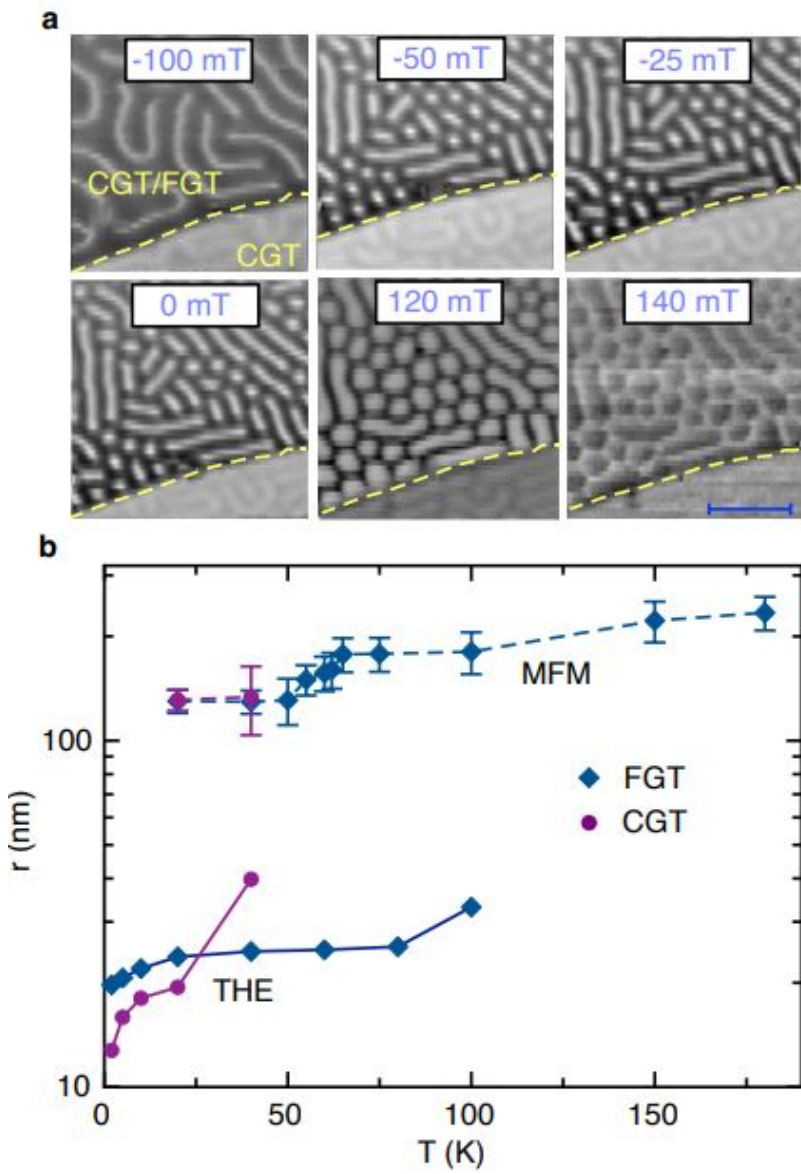
Figure 4.4: Magnetic skyrmions showing up as a function of magnetic field (even at zero field) and skyrmion size dependence on the temperature. a, Skyrmion lattice on CGT side at 20 K. Scale bar: 1 μm. b, Skyrmion size extracted from topological Hall effect (an order-of-magnitude estimate) and from magnetic force microscopy images.

4.1.5 Expanding on the Data

A more detailed account of the skyrmion lattice formation on the CGT side of the heterostructure at 20 K can be seen in Fig 4.5. The sample is saturated with a large
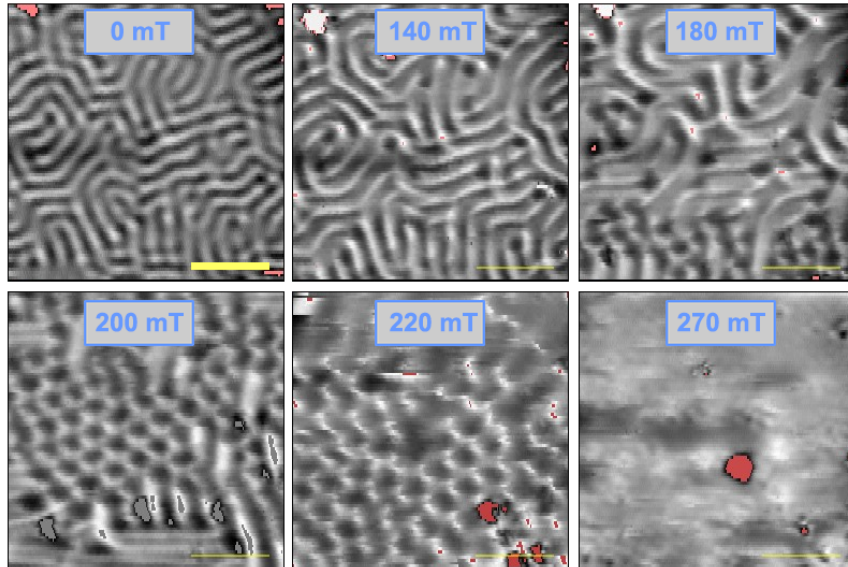
Figure 4.5: Skyrmion Lattice Formation and Evolution in CGT/FGT Heterostructure. Domains evolve from labyrinthine at zero field to labyrinths with few to many dots, eventually to a honeycomb lattice of skyrmions. The skyrmions are undetectable beyond 270 mT external field. Scale bar 2 μm

negative field of -9T, and then the external field is ramped upward. The zero field image shows the typical labyrinthine domains that are usually seen in these materials. At 140 mT we begin to see seemingly sporadic dot-like features appear among these labyrinthine domains. Further increasing the field to 180 mT we see a larger density of these dots until we reach 200 mT where they become tightly packed enough to form a honeycomb lattice. We see in the 220 mT image that increasing field increases the number of features as well as their size, but a source of noise or some other distortion to the features is introduced. Eventually the features are all but gone by the time external field reaches 270 mT.

4.1.6 Fourier Analysis of MFM Data

It would be beneficial to the case of labeling such features as skyrmions if we could find convincing evidence to their periodicity beyond visual inspection. A useful tool in this effort is the 2D Fast Fourier Transform (FFT). A 2D FFT would give us a spectrum of the spatial frequencies at which features recur in the original image, allowing us to rest assured that rather than sporadically placed dots these are features of regular size and placement, features more akin to skyrmions than unspecified magnetic bubble domains. The FFT spectra for a perfect honeycomb lattice of pont-like features would yield that same image back; the reciprocal lattice is itself. If we have some variation in the placement of these features, and when they have some measurable finite size, the spectra would look more like a doughnut or a ring with some separation from center [102]. An example can be seen in Fig 4.6.

With this in mind, we are equipped to interpret the Fourier spectra of the MFM images collected for the heterostructures. The images from Fig 4.5 are shown alongside their FFT spectra in Fig 4.7. The first point of interest is that the zero field image possesses a strong periodicity all its own, a dispersed ring with a finite radius to be exact. So the seemingly random labyrinthine domains are already possessing some order. As the skyrmions appear at 140 mT, and increase in number at 180 mT the strength of the Fourier signal increases (refer to the color bar inset along the left edge) while the radius decreases; that is, the labyrinthine domains occur periodically at a spatial frequency larger than the skyrmions. By 200 mT we have a honeycomb lattice of skyrmions, the ring in the Fourier spectra is at its strongest, but it may be difficult to differentiate from the noise that con-

47
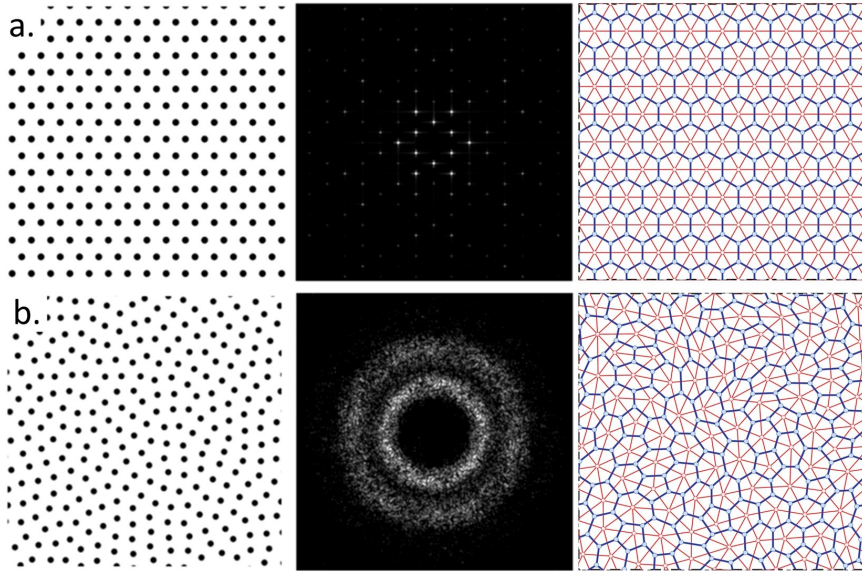
Figure 4.6: Example of Fourier Spectra. Top: An ideal triangular lattice yields another triangular lattice in the Fourier transform. Bottom: A distorted triangular lattice transforms into a ring-like feature in the Fourier transform. (From: Hyperuniform disordered waveguides and devices for near infrared silicon photonics by Milošević, M., et. al. http://creativecommons.org/licenses/by/4.0/).

tributes to the central gaussian. An example of almost pure noise resulting in the central gaussian can be seen in the 270 mT Fourier spectrum.

To further investigate the honeycomb lattice, we can filter out features in the 200 mT and 220 mT images by applying a mask to the central gaussian and performing an inverse Fourier transform, resulting in a filtered MFM image with whatever contributes to the central gaussian omitted. The results of this filtering are seen in Fig 4.8. When we mask out all but the strongest features a finite radius away from the central gaussian (a 2 sigma separation is used) we see the honeycomb lattice survives the inverse transform, indicating that this is what contributes most strongly to the Fourier features that are not
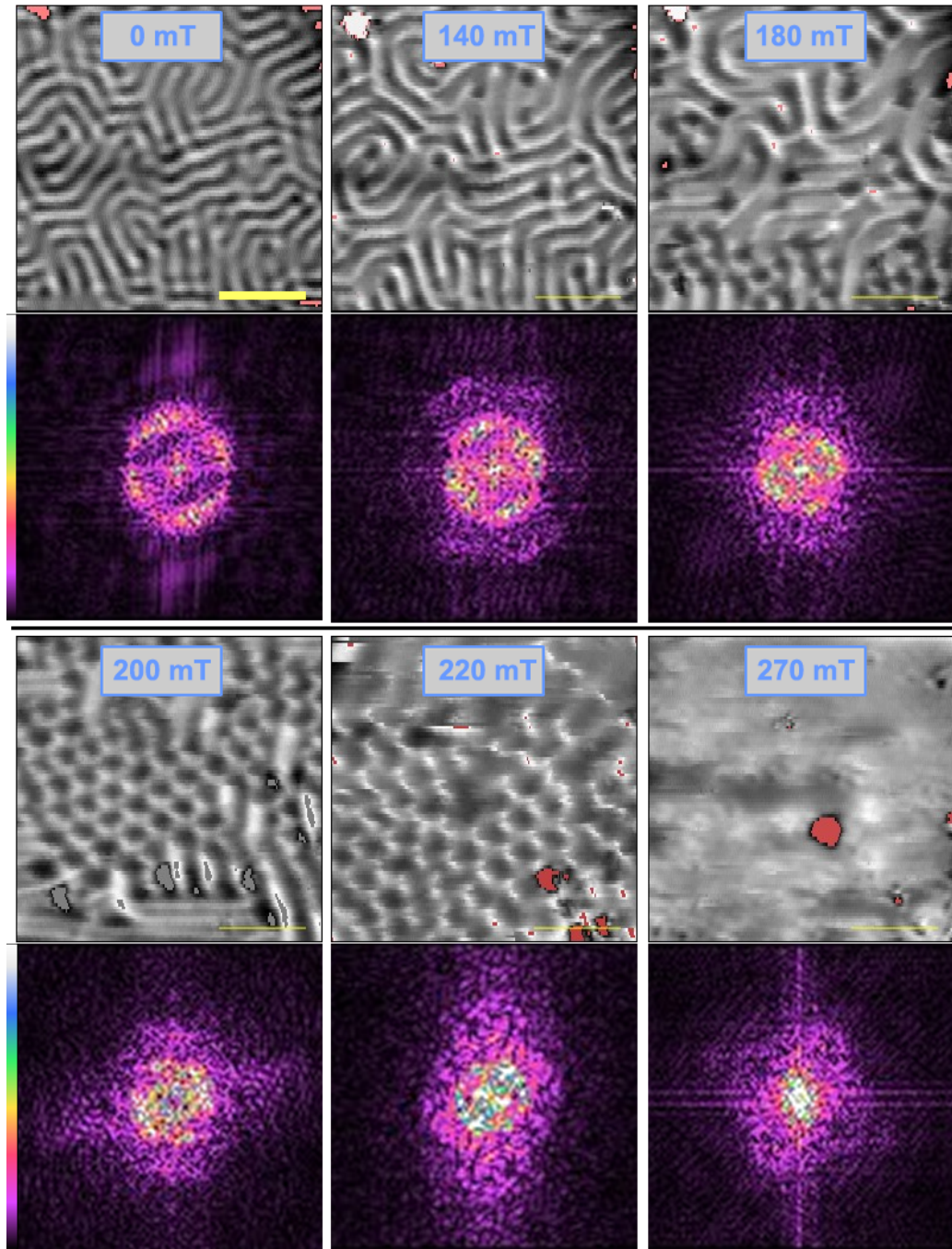
Figure 4.7: 2D Fourier Transforms of CGT/FGT Heterostructure MFM images. The labyrinthine domains show similar periodicity in a ring-like spectra, but the strength of the feature increases as the lattice forms, though noise is introduced. The nearly flat response MFM image yields the expected result of nearing a 2D Gaussian.
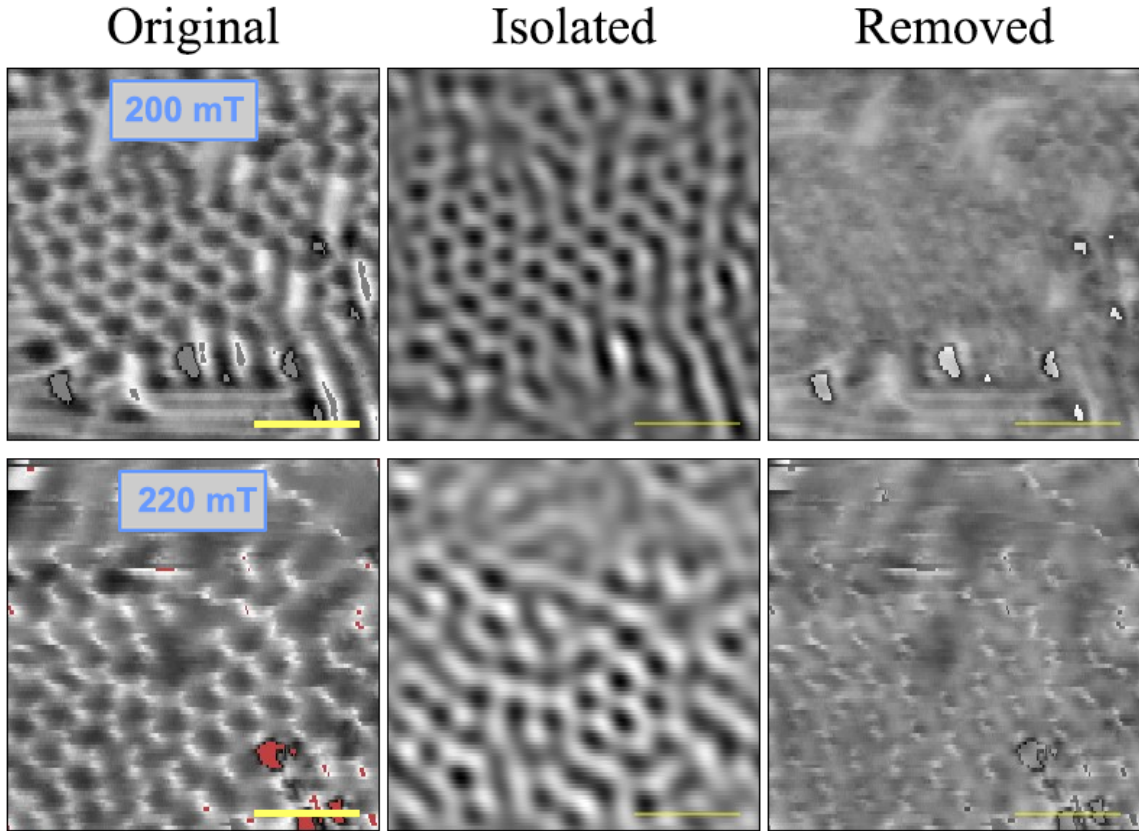
Figure 4.8: Fourier Filtering of Skyrmion Lattice. The original MFM images are shown to the left, the center images are the result of the inverse Fourier transform of the targeted features, the right images are the inverse Fourier transform of the omitted features. Scale bars are 2 μm.

the central gaussian. The omitted features in the right images show that it is mostly noise and artifacts that have been ignored.

It should be noted that the DMI can facilitate and stabilize features other than dot-like skyrmions. It has been shown previously that FGT systems with emergent DMI that anisotropic stripes occur. Lorentz Transmission Electron Microscopy (LTEM) shows these stripes possess Néel type domain walls and are therefore chiral in nature [94]. We see
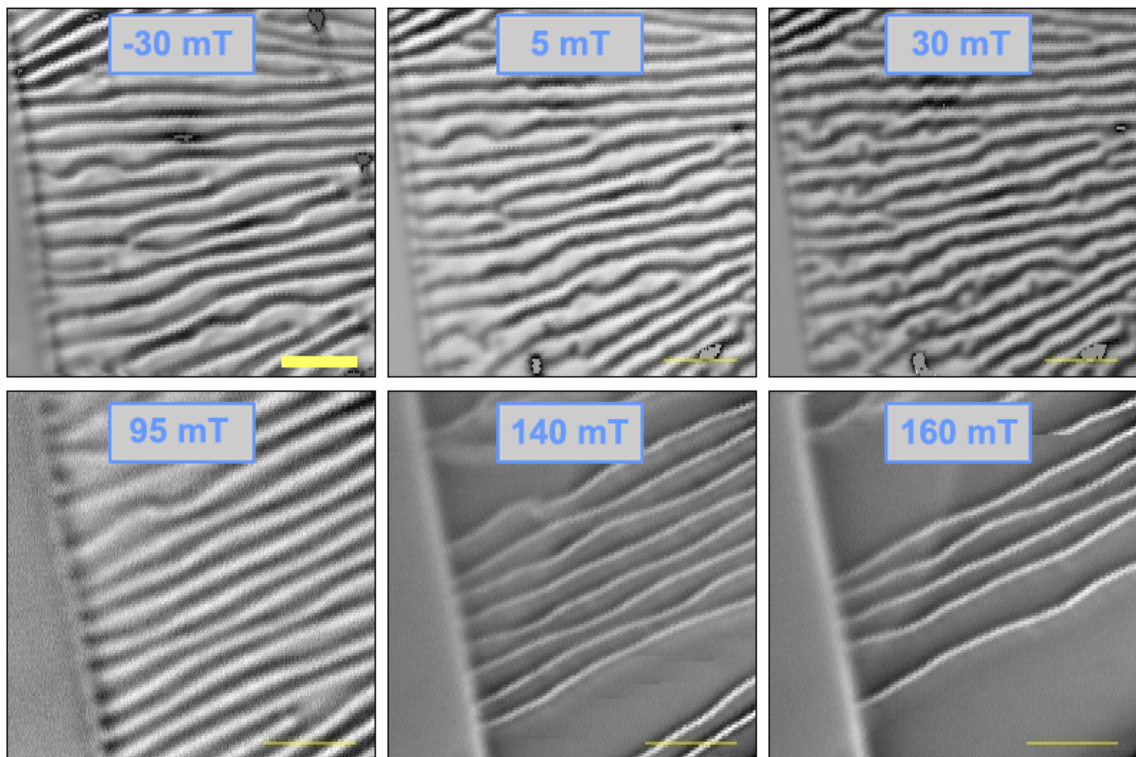
Figure 4.9: Stripe Domains in FGT/CGT at 20K. Stripes appear at low negative field after saturating at large negative field (-9 T) and persist until 95 mT. Some stripes disappear at 140 mT and even more at 160 mT. Saturation to single domain occurs between 160 and 170 mT. Scale bar is 1μm.
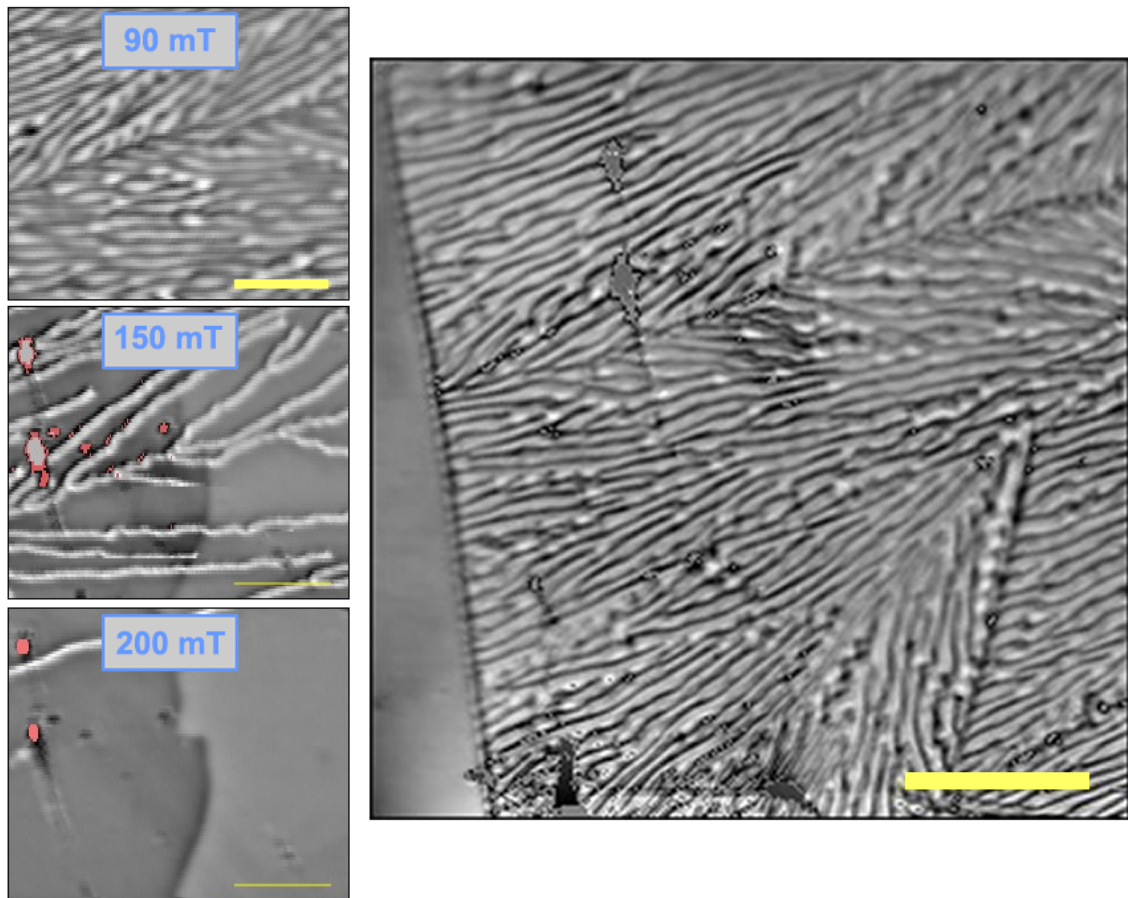
Figure 4.10: Domain Evolution in FGT/FGT at T = 45 K. Left (column): Stripes evolve as magnetic field is increased. Scale bar is 2 μm. Right (single): A large region of the sample at 60 mT. Scale bar is 3 μm.

such stripes in our FGT/CGT heterostructure (FGT atop CGT). In Fig 4.9 we can see the evolution of such stripes as magnetic field is increased at T = 20 K. The stripes appear as early as -30 mT after saturation at large negative field (9 T) and persist until about 140 mT where they begin to thin out and eventually the system enters the single domain state beyond 160 mT. In Fig 4.10 we see the evolution of the stripes at T = 45K, where they no longer align along the same direction, but seem to have two preferred directions with a clear separation of domains where stripes prefer one direction in one domain and another direction in the other. There is no topographical feature corresponding to this domain wall. It is possible that domains like this existed in the T = 20 K case, as it was later observed that different regions of sample exhibited different formations, but time constraints had us keep the region of interest fixed. We see in Fig 4.11 that the system defaults to its labyrinthine domains when the temperature goes above the T_C of CGT at T = 75 K. So the anisotropic stripe domains are dependent upon the magnetic state of the underlying CGT. The Fourier spectra for the T = 45 K and T = 20 K images with the strongest stripe features are shown in Fig 4.12 and should be noted for comparison with the images in the next section for the Fe_x-TaS_2 sample.

An interesting bit to note here is that there seem to be two sets of of periodic, nonrandom features contributing to the FFT spectra in both the 20 K and 40 K cases. When we isolate peak features 2 σ from the central gaussian we see that these correspond to the prominent stripe pattern from the original image, but there are peaks that are isolated and separate from center in the omitted features image as well. One possibility is that we are imaging strip domains throughout the FGT flake while skyrmions form at the interface
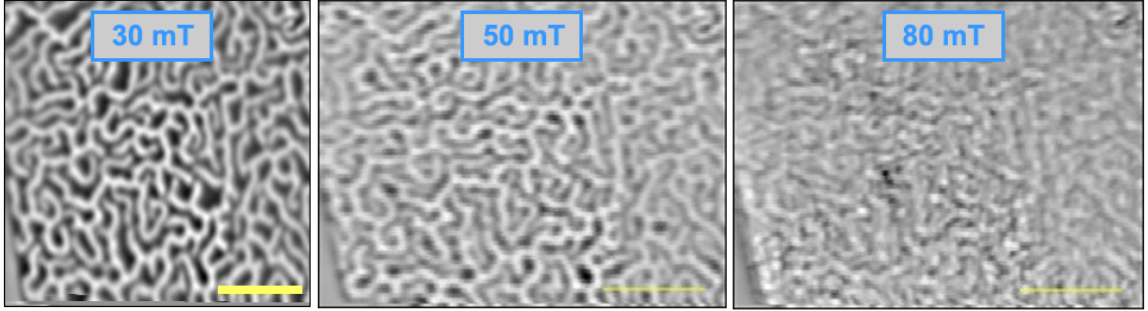
Figure 4.11: Domain structure of FGT/CGT at 75 K. The stripe domains are not present above the T_C of CGT and do not form before saturation occurs. Scale bars are all 2µm.

within the underlying CGT, and the warping of the stripes at particular fields are not actually the strip domains undergoing any change but the underlying skyrmions summing their stray fields with those of the top area stripes. We understand this effect to be possible due to the long-range nature of the magnetic probe.

4.1.7 Summary and Outlook

We explored the ultrathin FGT/CGT heterostructures as a platform for hosting small and tunable two groups of magnetic skyrmions. In this system, the inversion symmetry breaking near the FGT/CGT interface gives rise to an emergent DMI, thereby creating robust magnetic skyrmions. By harnessing the interface between two vdW ferromagnets, we achieved magnetic skyrmions on two sides of an interface.

The multi groups of skyrmions in FGT/CGT heterostructures allow versatility when designing and fabricating skyrmion-based devices. Due to the atomically thin nature of vdW materials and their easy control by electrical gating, one can foresee manipulating the skyrmions on each side with dual electric gating by which the skyrmion phase can be
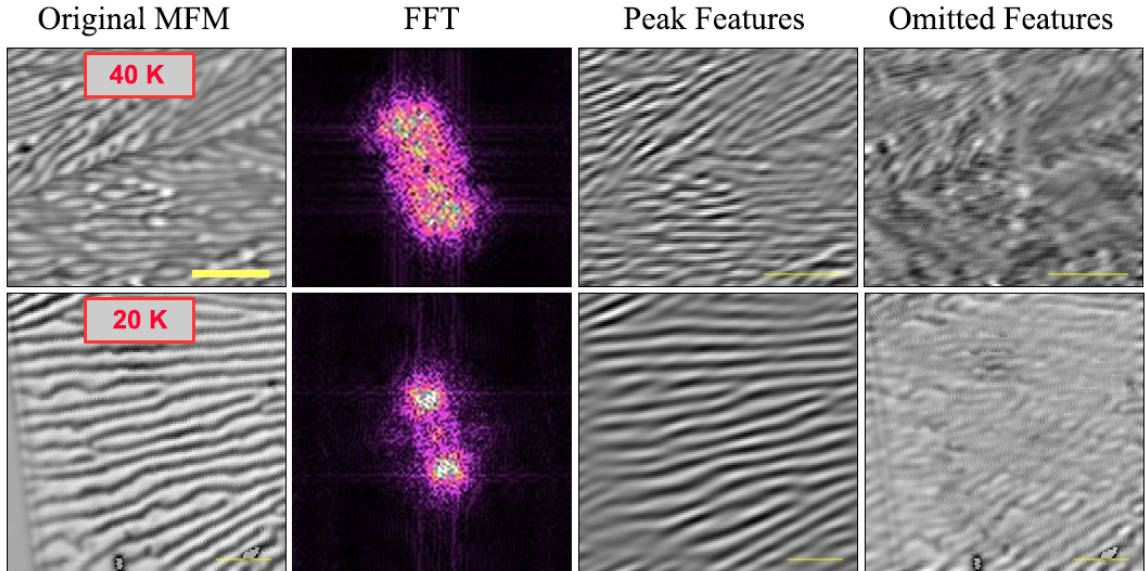
Figure 4.12: FFT Spectra for Stripe Domains at 20 K and 40 K. When peak features 2 sigma from center are targeted it appears to be a superposition of two sets of features.

turned on or off. Furthermore, the twist angle between FGT and CGT may be tuned, where a new functionality could be added for manipulating skyrmions in atomically thin vdW heterostructures. With an accurate determination of twist angle between FGT and CGT layers, magnetic skyrmions from DMI or Moiré pattern may be differentiated. This versatile advantage offers a fertile playground for exploring emergent phenomena arising from hybrid interfaces, leading to magnetic skyrmions with additional functionalities.

4.1.8 MFM Details

The MFM measurements were performed in a home-built low-temperature scanning probe microscope using commercial MFM probes (Bruker MESPV2) with a spring constant of $k = 3$ N m^{-1} , a resonance frequency $f_0 \sim 75$ kHz, and a Co-Cr magnetic coating. MFM images were taken in a constant height mode with the tip scanning plane at $\sim$

100 nm above the sample surface. The MFM signal, the change in the resonance frequency, is measured by a Nanonis SPM Controller using a phase-lock loop. The magnetic moment of the probe is nominally in the order of 10^{-16} A m^2 .

4.2 Imaging Domains within Fe$_{1/3}$TaS$_2$

4.2.1 Introduction

A category of particular interest in layered van der Waals materials is that of the transition-metal dichalcogenide (TMD). As their name suggests, these van der Waals materials consist of a transition metal ion strongly bonded to two of the same atom from the chalcogen column of elements. The three atomic planes form a honeycomb lattice with threefold symmetry and the possibility of mirror and/or inversion symmetry [103]. The array of intriguing properties presented by TMDs is expanded with the intercalation of new atoms within the van der Waals gaps of their structures [104, 105], particularly the introduction of a 3d-element such as Fe into a tantallum TMD such as TaS$_2$ can introduce long-range magnetic ordering that was otherwise absent [106].

4.2.2 Fe-Doped TaS$_2$

The doping of Fe into TaS$_2$ at different concentrations can bring about different phenomena corresponding to the symmetries offered by the level of doping. For a baseline, we may refer to two commensurate values of $x = 1/4$ or $1/3$ for the compound Fe$_x$TaS$_2$, where for every $1/x$ unit cells, 1 will have an Fe atom within the van der Waals gap. In one of these ideal cases of $x = 1/4$ resulting in Fe$_{1/4}$TaS$_2$, previous works have observed hard

ferromagnetism with perpendicular magnetic anisotropy (easy-axis along c-axis) with sharp switching at low temperatures when coercive field H_C is approached [107, 108, 109]. This sharp switching can be softened when introducing iron in excess of $x = 1/4$, indicating that stoichiometry influences the magnetic ordering [109].

Of particular note is the ideal concentration of $x = 1/3$ in $Fe_{1/3}TaS_2$, where the hexagonal structure of 2H-type TaS_2 along with the newly introduced Fe atoms belong to the noncentrosymmetric chiral space group $P6_322$ [110]. This breaking of the inversion symmetry regularly present in TaS_2 and $Fe_{1/4}TaS_2$ creates an environment in with the antisymmetric exchange interaction known as the Dzyaloshinskii–Moriya interaction (DMI) can emerge [111, 112, 43] and the possibility to observe topological phenomena is presented.

In the results presented below, we observe signatures of the Topological Hall Effect (THE) in the magnetotransport measurements of bulk $Fe_{1/3}TaS_2$, indicating the possible presence of topological magnetic textures within the sample. This is further investigated by the imaging technique Magnetic Force Microscopy (MFM), where a magnetic cantilever probe is rastered across the bulk, interacting with the stray fields originating from the spins within and imaging the shift in its resonance frequency from these interactions. Periodic, regularly shaped features are detected and their regularity and periodicity are confirmed with the fast Fourier Transform (FFT) spatial frequency analysis method. These observations point to the existence of skyrmions within bulk $Fe_{1/3}TaS_2$ which are not observed in other concentrations of Fe_xTaS_2.
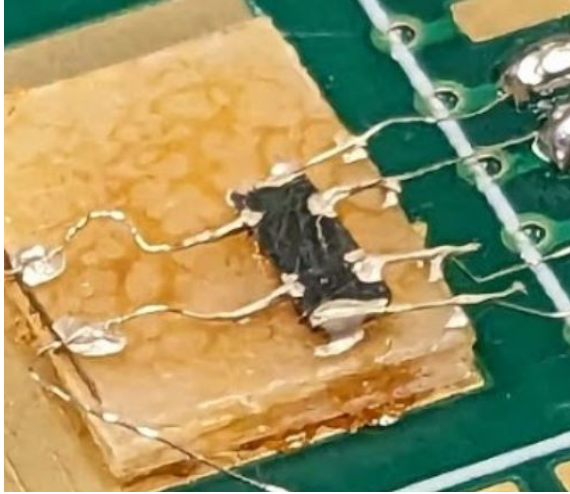
Figure 4.13: $Fe_{1/3}$-TaS_2 Sample 132A on the PCB Board arranged for Hall Resistivity Measurement

4.2.3 Analyzing the THE Signal

Two bulk samples of $Fe_{1/3}TaS_2$ were prepared for Hall resistivity measurements by soldering thin conductive wire to the ends of a rectangular sample in a Hall probe configuration as seen in Fig 4.13. A Current of $I_{ab} = $ was sent through the sample within the a-b plane with probes arranged perpendicular to the current measuring voltage V_{xy}. An external magnetic field, H_{EXT} parallel to the c-axis was ramped from -9 T to +9 T. The results are pictured in Fig 4.14. The Hall voltage (proportional to the Hall resistivity) shows contributions from both the classical Hall Effect and Anomalous Hall Effect (AHE) as seen by the linear skew of the overall plot and the signature of hard magnetic switching at coercive field B (near 3 T for 5K and 2 T for 10K). At the hard switching we see signatures of the Topological Hall Effect (THE) in the anticipatory dips and peaks just before the switch as well as the slight overshoot of saturation magnetization M_S just at the end of switching.
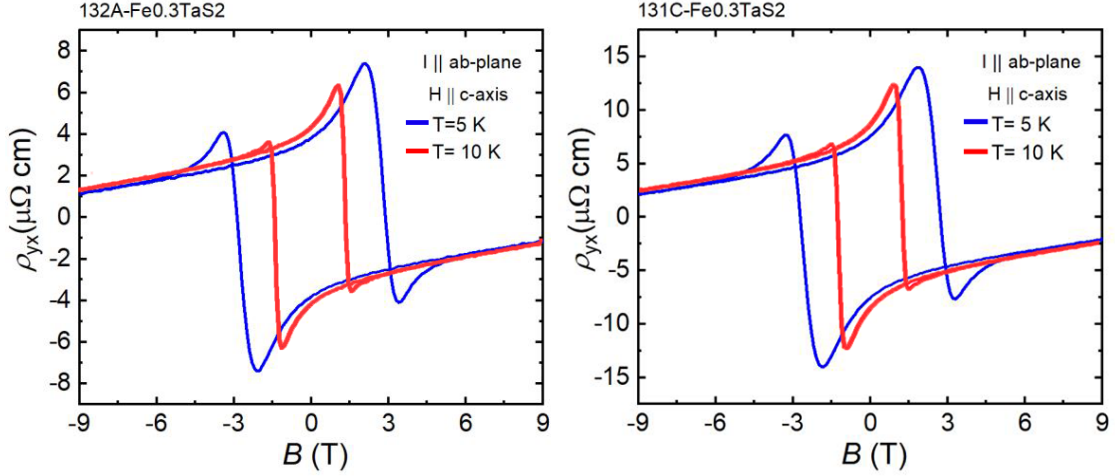
Figure 4.14: Transport measurement data from $Fe_{1/3}$-TaS_2 Samples 131C and 132A. Measurements taken at 5K and 10K with external field parallel to sample c-axis

4.2.4 Directly Imaging Domain Formation with MFM

To further examine the origin of THE arising within the bulk $Fe_{1/3}TaS_2$, we performed low-temperature MFM measurements under applied magnetic fields (resolution of the MFM measurement can be found in 3). Fig 4.15 shows a series of MFM images taken on the 162 μm $Fe_{1/3}TaS_2$ device (pictured in Fig 4.13) with applied perpendicular magnetic fields at 8K. The sample is first saturated to a high field of 9 T, as the field is brought down toward 0 T and beyond magnetic domains begin to form. At $H_{ext} = 2$ T we begin to see regularly sized features that appear in a periodic spacing. Upon further decreasing the field we see at $H_{ext} = -5$ T that the smaller features all but disappear and we are left with larger features that may belong to a stripe-like set of domains. These features appear much more weakly than typical topological textures imaged in few-layer van der Waals materials. These could be due to two main reasons: the skyrmions are occurring in 3D space and
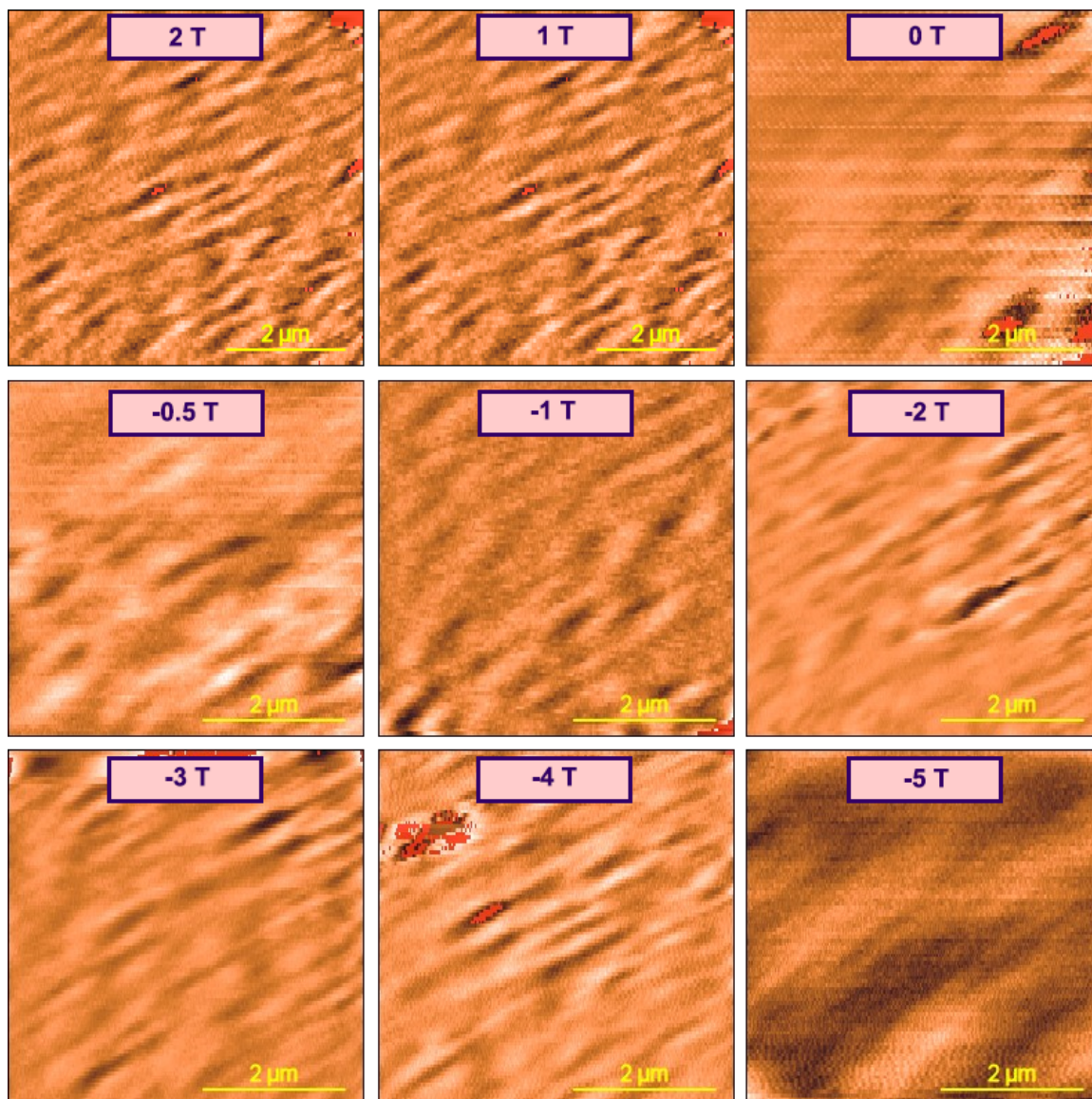
Figure 4.15: A series of MFM images on $Fe_{1/3}$-TaS_2 with ramping magnetic field. The sample was saturated with 9 T external field, images were taken at field intervals as field was ramped downward. Features appear in the low positive fields approaching zero field where they nearly disappear before reemerging as the negative coercive field is approached. The features are gone after the transition point indicated by transport measurements.

are not confined to a 2D plane, so the formation of a skyrmion lattice is more difficult to image as it is not guaranteed that the entirety of the bulk is forming such features and they may be screened by larger domains in the upper layers of sample [113]. Secondly, the top most layers could be arranged in their own domains that distort the images made of the underlying skyrmions. It is seen in Fig 4.13 that after the skyrmionic features are washed out at -5 T that there remain larger, stripe-like domains, the signals from which would be stronger if they exist on the layers in closer proximity to the probe.

As a means of control, we performed the same measurement on a sample of $Fe_{1/4}TaS_2$, that is Fe-doped TaS_2 where the Fe concentration is 1 Fe atom for every 4 unit cells. Aside from topographic anomalies effecting the signal, the MFM shows a signature of a multidomain state present in the bulk; however, it is one of seemingly random orientation and domain shape (see Fig 4.16. Again, the sample was saturated at a high magnetic field and images were taken at increments of decreasing magnetic field. We see that at the transition field range (between -2 T and -5 T) that we see no interesting domain formation. There perhaps exists multiple domains, but there is no obvious periodicity or regularity to their structure. To further investigate this, we can use the FFT analysis from earlier in this chapter.

4.2.5 FFT Filtering the MFM Images

Due to the complications of imaging magnetic domains that occur within a bulk material, we need to devise a way to focus on the features from the noise of the rest of the bulk. We again can turn to the Fourier analysis. By performing a fast Fourier transform
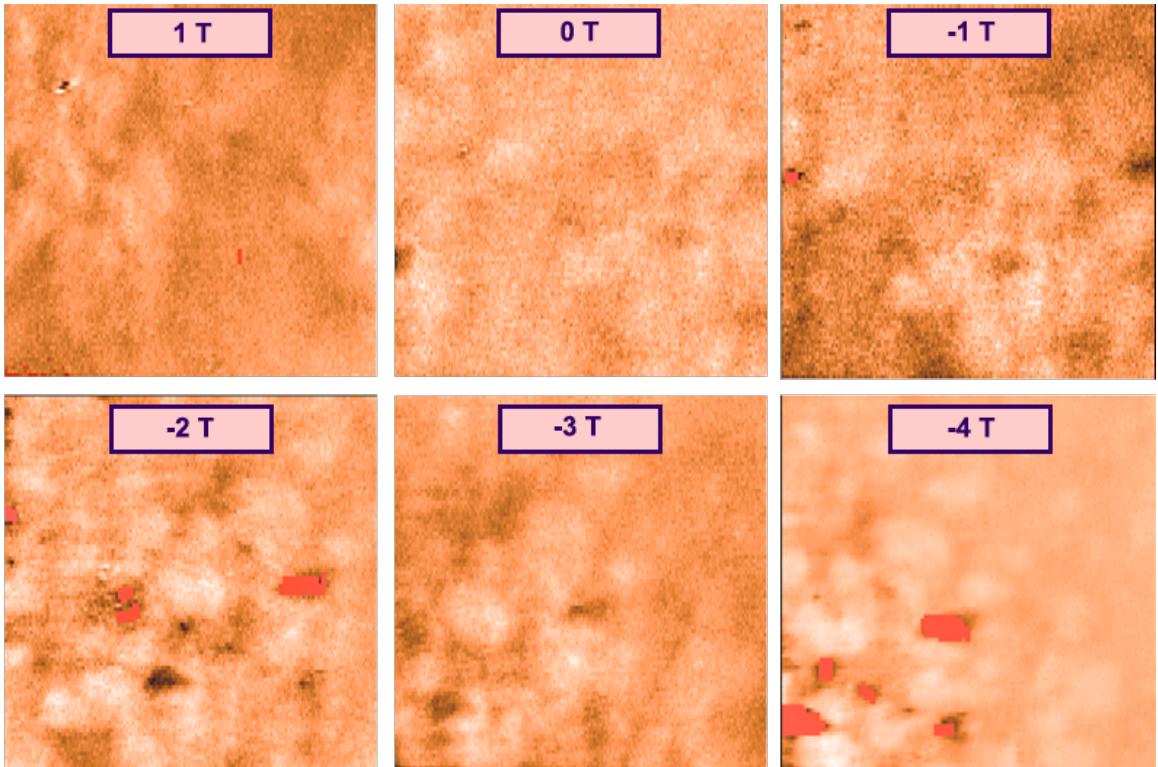
Figure 4.16: The MFM images for the $Fe_{1/4}$-TaS_2 sample at key field values. The sample was saturated at a large negative field (-9 T) before the field was ramped up as images were taken. There are no features of note beyond those affected by topography. There is a multidomain state visible at -1 T, but it quickly saturates and looks nothing like the multidomain states accessible in $Fe_{1/3}$-TaS_2.
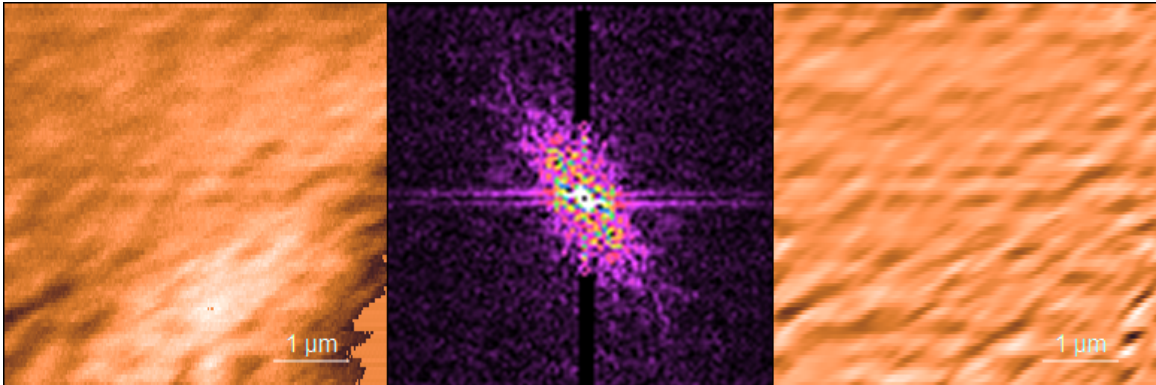
Figure 4.17: An example of using 2D Fast Fourier Transform filtering on an MFM image. Left: Raw MFM data. Center: FFT of MFM data. Right: MFM data filtered from FFT

(FFT) on the spatial MFM data, we can categorize the features by periodicity. Using a set of criteria to ignore artifacts and random noise (we ignore the central most peak in the FFT which will correspond to a frequency of zero, as well as scan direction and piezo drift artifacts which show up as vertical and horizontal stripes) we can create a region of interest (ROI) in the FFT spectra, then perform an inverse FFT to retrieve a real space MFM image that corresponds only to the underlying magnetic domains, instrumental artifacts and random noise excluded, an example can be seen in Fig 4.17.

Aside from its role as an image filter, the FFT spectra itself should be noted for each image. As discussed earlier in section 4.1 we can interpret the nature of the periodicity of the features with this spectra. The random noise across the image will show up as a contribution to the central $(0, 0)$ centered peak in the FFT spectra, whereas the far outliers in the spectra are representative of singular features scattered about the image. It's the area surrounding the central peak that is of interest; features that are removed enough from the central peak as to not be direct contributions to it, but close enough that they are not

among the outliers. We saw the near ideal case in section 4.1, a dispersed ring at a finite distance from the center indicated the presence of a distorted hexagonal lattice. Here, our images from the $Fe_{1/3}$-TaS_2 yield two distinct symmetric peaks separate from the central noise peak, located in quadrants 2 and 4 if the FFT spectra is viewed from the perspective of a typical 2D x-y plane (the (-x, +y) and (+x, -y) quadrants). Conversely, the FFT images generated from the $Fe_{1/4}$-TaS_2 sample, while they vary in exact size and shape, are simply 2D Gaussian peaks centered at origin. From comparing these sets of FFT spectra we have determined that the multidomain states present in each compound differ in the category of periodicity.

4.2.6 Summary and Conclusion

We have seen clearly that a multidomain state exists in the Fe-doped TaS_2 with a concentration of $Fe_{1/3}$ that does not exist in the $Fe_{1/4}$ concentration. This multidomain state appears as a periodic array of regularly sized features that, when compared to the THE signal present in the transport data may be interpreted to be skyrmions. The reasoning to label these features as topological in nature is their periodic arrangement coupled with their occurrence at the fields coinciding with the topological Hall signal in transport measurements. It is hypothesized that this particular concentration of Fe-doped TaS_2 gives rise to such features because of its broken inversion symmetry opening the doors for the DMI to introduce antisymmetric exchange between neighboring spins, thus coercing the formation of skyrmions. Adjusting magnetic doping to induce topological features unlocks avenues to observe topological phenomena that are more accessible than intrinsic van der Waals magnets, removing the need for clean interfaces or vacancy- or imperfection-free crystals to bring these features about.

Chapter 5

Torque Differential Magnetometry and Interlayer Exchange

5.1 Preliminary Results

Using an experimental setup similar to that described in Chapter 3, we performed tuning fork torque differential magnetometry measurements in a Quantum Design Physical Property Measurement System (PPMS) using a stepper motor controlled rotating insert. Fig 5.1 shows the sample space of the insert. The sample stage is rotated from 0-360º by a gear assembly attached to a rod which runs through the center of the insert to the top where it rests outside of the PPMS cryostat. A stepper motor assembly called the rotator head is attached to the top and rotates the sample via rotation of the inner rod (See Fig 5.2). A tuning fork was prepared by epoxying it to a ceramic base which was epoxied atop a ThorLabs piezoelectric chip. The piezo chip was driven with an oscillating AC voltage to

Figure 5.1: The PPMS Rotator Insert. Left: The PPMS rotator insert sample space with coaxial cables fed through. Right: The rotator sample space with tuning fork in qPlus configuration.

Figure 5.2: The rotator head containing stepper motor for insert.
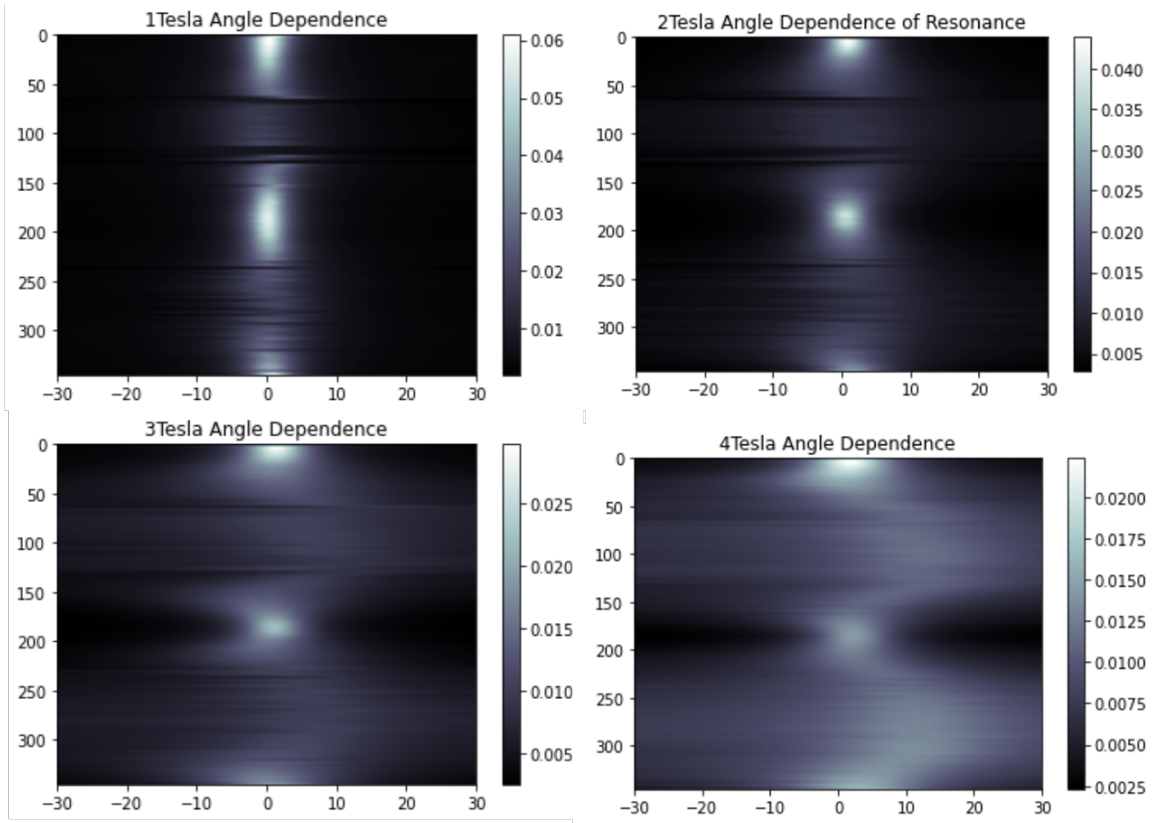
Figure 5.3: Preliminary results for torque differential magnetometry (TDM) measurements.

"shake" the tuning fork at resonance, which was wired to read the output current to track the oscillations. A chunk of van der Waals ferromagnet Fe_3GeTe_2 was glued to the end of one prong (see Fig 3.7).

Using a custom LabVIEW VI and scripts written in python, the PPMS rotator system was set to measure the resonant frequency of the tuning fork by sweeping +/- 30 Hz from resonance at set angles between 0 and 360º for magnetic field values which incremented from 0 to 4 T, allowing us to use these parameters to find phase shift Δf_0 as a function of
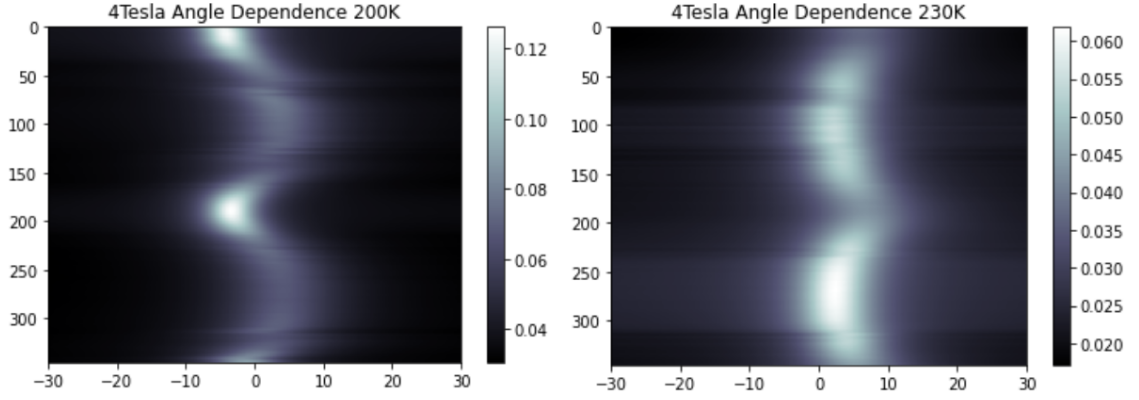
Figure 5.4: 200k and 230K TDM results for field of 4 T

H_{ext} and θ, $\Delta f_0(H_{ext}, \theta)$. The preliminary results of these measurements are found in Fig 5.3.

In order to find the frequency shift to apply to the frequency-dependent angle measurement we should treat each frequency sweep as a Lorentzian distribution. We can fit parameters of each peack using the general form,

$$L(x; y_0, y_{max}, x_0, w) = y_0 + \frac{y_{max}}{\pi}\left[\frac{w}{(x - x_0)^2 + w^2}\right] \tag{5.1}$$

where y_0 is the baseline value, x_0 is the center value of the Lorentzian peak, y_{max} is the peak value of the Lorentzian, and w is the width measured at half y_0. See Fig 5.6 for labels on an arbirtrary Lorentzian distribution.
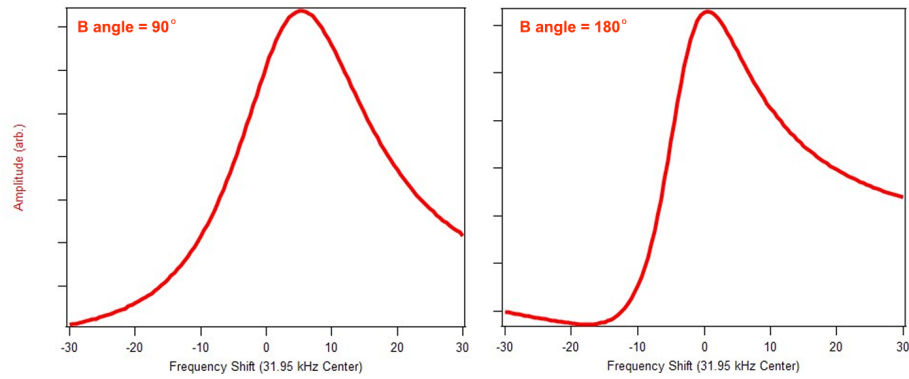
Figure 5.5: Two Linecuts from the Magnetometry Data. Line cuts at 90° and 180° to highlight the difference in line shapes at extreme values.
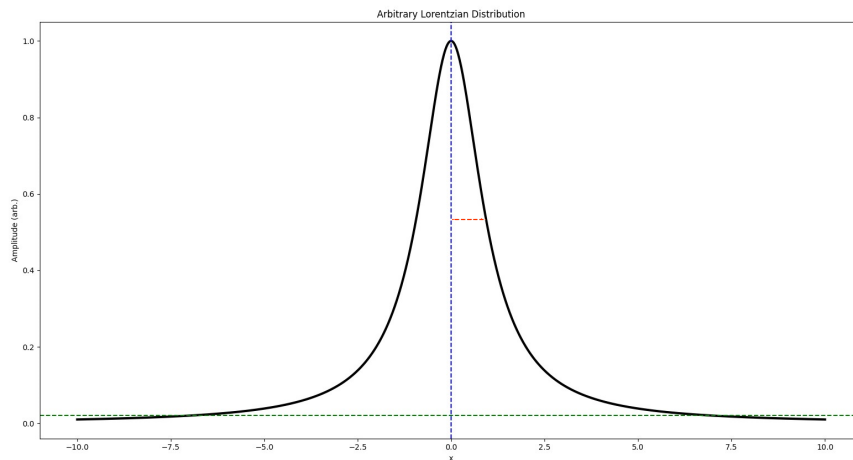
Figure 5.6: Sample Lorentzian with Fitting Parameters. Baseline value, y_0 noted with dashed green line, center value x_0 noted with vertical dashed blue line, width, w indicated by dashed red line.

5.2 Summary and Future Experiments

The measurements were short-lived, hence the dataset is not very robust. We needed to move to another PPMS setup which required use to provide our own means to drive the rotator head on the insert and provide leak protection to the insert with home grown solutions. Interestingly, the original dataset did have two instances of data to put our eyes on, those of 200K and 230K angle dependence at 4 T field seen in Fig 5.4. We can see two symmetric and incremental shifts in frequency occurring between the strongest peaks at 0 and 180°. These measurements were done in the standard two-prong oscillation mode of the QTF. We look forward to performing this measurement in qPlus mode and with more exotic magnetic systems.

Chapter 6

New Insights

6.1   Fe-Vacancies Contribute to Broken Inversion Symmetry

In recent work with Fe_3GTe_2, researchers have found that introducing iron vacancies can contribute to breaking inversion symmetry in the system. Fe-deficient $Fe_{2.9}GeTe_2$ and $Fe_{2.8}GeTe_2$ were probed via second harmonic generation technique [114]. Light was shone on the samples at two polarizations, 45° and 0° with respect to the surface, intensity of the 2ω reflected light was plotted as a function of sample rotation. The tell-tale sign of symmetry breaking is a high intensity three petal feature in the polar plot, with the 0° mode yielding a low intensity isotropic result. Moreover, the results show that while the $Fe_{2.8}GeTe_2$ sample shows the strongest signal of symmetry breaking, there exists a faint signature of the same effect in $Fe_{2.9}GeTe_2$ and Fe_3GeTe_2, showing that FGT's inversion symmetry may be broken inherently, see Fig 6.1. This sheds new light on the origins of
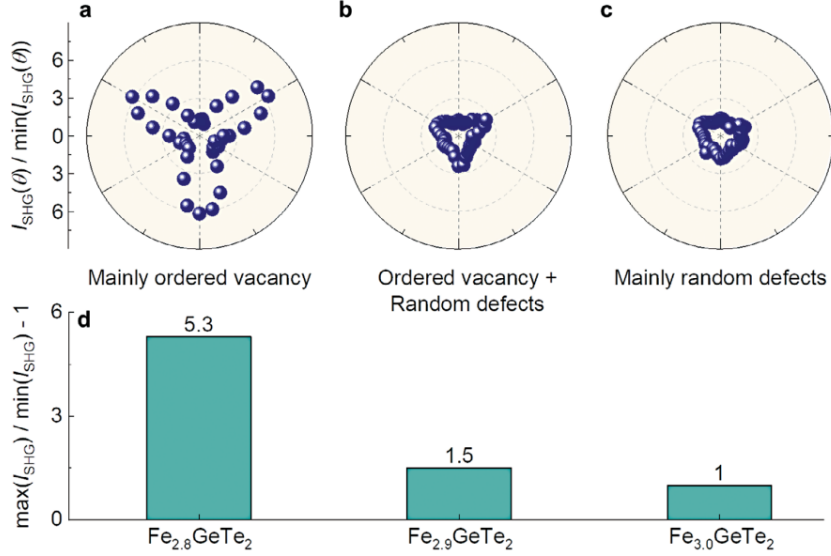
Figure 6.1: SHG evoution on Fe-deficiency.a-c, Three petal feature most prominent in $Fe_{2.8}GeTe_2$, but faintly present in $Fe_{2.9}GeTe_2$ and even Fe_3GeTe_2. d, Relative sharpness of each SHG normalized plot. (From Broken Inversion Symmetry in Van Der Waals Topological Ferromagnetic Metal Iron Germanium Telluride, by Zhang, K-X., et. al., used with publisher's permission).

FGT's spin-orbit coupling as well as the ways by which topological features may be stabilized in the system.

6.2   Fe-Vacancies Present in Pristine FGT

A recent X-ray Diffraction (XRD) study has performed goodness of fit(GOF) parameter mapping across a sample of FGT regarding the positions of Fe atoms adjacent to Ge atoms in the FGT crystal structure [115]. Fig 6.2 shows the rsults in a contour map. Regions of low GOF indicate areas of misaligned or missing Fe atoms in the designated position. This sample of stoichiometrically prepared FGT was able to host Néel skyrmions without the introduction of a heterostructure or oxidized layer. This is more evidence
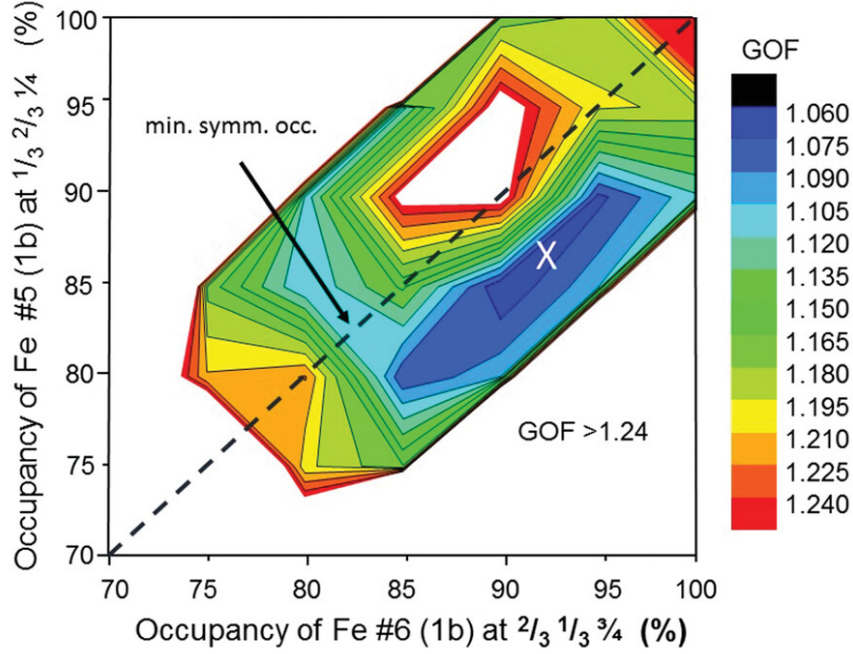
Figure 6.2: Contour map of GOF versus site occupancies of Fe atoms #5 and #6. The global minimum is indicated by the white cross. The dashed diagonal indicates the condition $\Theta(5) = \Theta(6)$ in the case of a centrosymmetric space group for which a local minimum at $\Theta = 0.83$ is found. The white area corresponds to the condition GOF ¿ 1.24. (From Magnetic Skyrmions in a Thickness Tunable 2D Ferromagnet from a Defect Driven Dzyaloshinskii–Moriya Interaction, by Chakraborty, A., et. al., open access article distributed under the terms of the Creative Commons CC BY license)

that FGT alone may be able to host many unique topological phenomena under certain conditions.

6.3 The Future of vdW Magnetism

Among the many systems and materials on the horizon for van der Waals magnetism are two materials I would like to briefly highlight here; the family of topological insulator antiferromagnets $MnBi_{2+2n}Te_{4+3n}$ (MBT) and the room temperature itinerant ferromagnet Fe_3GaTe_2 (FGaT).

75

Among the many attractive features of a topological magnetic van der Waals material, one obvious one is possibility for the Quantum Anomalous Hall Effect (QAHE), which has been reported in MBT in the past [41]. More interestingly though, MBT is a family of materials, septuple layers (SLs) of $MnBi_2Te_4$ stacked with topological insulator Bi_2Te_3, the quintuple layer (QL). With the magnetic moment provided by the Mn ion, this spacing with the QLs increases the distance between magnetic moments and therefore decreases the interlayer coupling strength between SLs [37]. This tunability of exchange interaction makes for a veritable playground for correlated electron related physics and topological magnetic phenomena.

Room temperature ferromagnet Fe_3GaTe_2 (FGaT) shares many properties with Fe_3GeTe_2 [116]. FGaT possesses strong spin-orbit coupling, strong perpendicular magnetic anisotropy and ferromagnetic coupling. It, too has a relatively high transition temperature, just as FGT was known for, but FGaT transitions above room temperature at close to $T_C = 350K$. Since its emergence in the field, many of the works done with FGT are being repeated on FGaT, opening the door to a somewhat familiar yet exciting area to explore.

Chapter 7

Conclusions

The works I have presented here uncovered many interesting secrets of the materials Fe_3GeTe_2, $Cr_2Ge_2Te_6$, and Fe_x-TaS_2. More importantly, the works have not fully explained each phenomena, but have led to further questions that require answering, especially when considering the more recent work of other researchers. I would like to see more topological textures images in FGT alone, under various circumstances. Thickness dependence of feature size would be an interesting thing to bring to the table for systems without heterostructure or other assistance in breaking symmetry.

For Fe_x-TaS_2, more work needs to be done in even the current study underway. Temperature dependence on the $x = 1/3$ sample to show the features disappear with the loss of magnetic ordering is necessary. Thickness dependence and even few-layer measurements can provide insight and clearer imaging of the magnetic domains as well. Do the features exist in the in-between concentrations of $1/4 < x < 1/3$? All of these scenarios would be interesting to pursue.

My tuning fork magnetometry measurement was always meant to target MBT and its interlayer exchange coupling. In the coming weeks after publishing this I hope to begin that measurement, or at least work everything out so a future student can jump right into it.

As with all things, the MFM setup in our lab can be improved upon. A big problem is the probe and fiber being perfectly aligned at room temperature, but losing alignment during loading and cooldown. With no way to adjust this, the only solution is to unload the sample and redo everything, a very lengthy and wasteful process. It might be a bit ambitious, but an array of piezoelectric chips could provide fine tuning of either fiber or cantilever position. An alternate route for improvement is to meticulously design and machine a cantilever seating onto the probe holder.

With questions unanswered and improvements in mind, the study of van der Waals magnetism appears as though it plans on sticking around for a while.

Bibliography

[1] N. Mounet, M. Gibertini, D. Campil P. Schwaller, A. Marrazzo A. Merkys, T. Sohier, I. E. Castelli, A. Cepellotti, G. Pizzi, and N. Marzari. Two-dimensional materials from high-throughput computational exfoliation of experimentally known compounds. *Nature Nanotechnology*, 13:246–252, 2005.

[2] K. S. Novoselov, A. K. Geim, S. V. Morozov, D. Jiang, Y. Zhang, S. V. Dubonos, I. V. Grigorieva, and A. A. Firsov. Electric field effect in atomically thin carbon films. *Science*, 306(5696):666–669, 2004.

[3] Yuanbo Zhang, Yan-Wen Tan, Horst L. Stormer, and Philip Kim. Experimental observation of the quantum hall effect and berry's phase in graphene. *Nature*, 438(5696):201–204, 2005.

[4] V. Fatemi, S. Wu, Y. Cao, L. Bretheau, Q. D. Gibson, K. Watanabe, T. Taniguchi, R. J. Cava, and P. Jarillo-Herrero. Electrically tunable lowdensity superconductivity in a monolayer topological insulator. *Science*, 362(6417):926–929, 2018.

[5] V. Fatemi S. Wu, Q. D. Gibson, K. Watanabe, T. Taniguchi, R. J. Cava, and P. Jarillo-Herrero. Observation of the quantum spin hall effect up to 100 kelvin in a monolayer crystal. *Science*, 359(6371):76–79, 2018.

[6] K. F. Mak, J. Hone C. Lee, J. Shan, and T. F. Heinz. Atomically thin MoS_2: A new direct-gap semiconductor. *Phys. Rev. Lett.*, 105(136805), 2010.

[7] D. R. Klein, D. MacNeill, Q. Song, D. T. Larson, S. Fang, M. Xu, R. A. Ribeiro, P. C. Canfield, E. Kaxiras, R. Comin, and P. Jarillo-Herrero. Enhancement of interlayer exchange in an ultrathin two-dimensional magnet. *Nat. Phys.*, 15:1255–1260, 2019.

[8] X. Xi, W. Zhao Z. Wang, J.-H. Park, K. T. Law, H. Berger, L. Forró, J. Shan, and K. F. Mak. Ising pairing in superconducting $NbSe_2$. *Nat. Phys.*, 12:139–143, 2016.

[9] Y. Zhang, T.-T. Tang, C. Girit, Z. Hao, M. C. Martin, A. Zettl, M. F. Crommie, Y. R. Shen, and F. Wang. Direct observation of a widely tunable bandgap in bilayer graphene. *Nature*, 459:820–823, 2009.

[10] A. Avsar, J. Y. Tan, T. Taychatanapat, J. Balakrishnan, G.K.W. Koon, Y. Yeo, J. Lahiri, A. Carvalho, A. S. Rodin, E.C.T. O'Farrell, G. Eda, A. H. Castro Neto, and B. Özyilmaz. Spin–orbit proximity effect in graphene. *Nature Communications*, 5(1), September 2014.

[11] Zhe Wang, Dong–Keun Ki, Hua Chen, Helmuth Berger, Allan H. MacDonald, and Alberto F. Morpurgo. Strong interface-induced spin–orbit interaction in graphene on WS2. *Nature Communications*, 6(1), September 2015.

[12] Zhiyong Wang, Chi Tang, Raymond Sachs, Yafis Barlas, and Jing Shi. Proximity-induced ferromagnetism in graphene revealed by the anomalous hall effect. *Physical Review Letters*, 114(1), January 2015.

[13] Peng Wei, Sunwoo Lee, Florian Lemaitre, Lucas Pinel, Davide Cutaia, Wujoon Cha, Ferhat Katmis, Yu Zhu, Donald Heiman, James Hone, Jagadeesh S. Moodera, and Ching-Tzu Chen. Strong interfacial exchange field in the graphene/EuS heterostructure. *Nature Materials*, 15(7):711–716, March 2016.

[14] Ding Zhong, Kyle L. Seyler, Xiayu Linpeng, Ran Cheng, Nikhil Sivadas, Bevin Huang, Emma Schmidgall, Takashi Taniguchi, Kenji Watanabe, Michael A. McGuire, Wang Yao, Di Xiao, Kai-Mei C. Fu, and Xiaodong Xu. Van der waals engineering of ferromagnetic semiconductor heterostructures for spin and valleytronics. *Science Advances*, 3(5), May 2017.

[15] C. R. Dean, L. Wang, P. Maher, C. Forsythe, F. Ghahari, Y. Gao, J. Katoch, M. Ishigami, P. Moon, M. Koshino, T. Taniguchi, K. Watanabe, K. L. Shepard, J. Hone, and P. Kim. Hofstadter's butterfly and the fractal quantum hall effect in moiré superlattices. *Nature*, 497(7451):598–602, May 2013.

[16] B. Hunt, J. D. Sanchez-Yamagishi, A. F. Young, M. Yankowitz, B. J. LeRoy, K. Watanabe, T. Taniguchi, P. Moon, M. Koshino, P. Jarillo-Herrero, and R. C. Ashoori. Massive dirac fermions and hofstadter butterfly in a van der waals heterostructure. *Science*, 340(6139):1427–1430, June 2013.

[17] Yuan Cao, Valla Fatemi, Shiang Fang, Kenji Watanabe, Takashi Taniguchi, Efthimios Kaxiras, and Pablo Jarillo-Herrero. Unconventional superconductivity in magic-angle graphene superlattices. *Nature*, 556(7699):43–50, March 2018.

[18] Yuan Cao, Valla Fatemi, Ahmet Demir, Shiang Fang, Spencer L. Tomarken, Jason Y. Luo, Javier D. Sanchez-Yamagishi, Kenji Watanabe, Takashi Taniguchi, Efthimios Kaxiras, Ray C. Ashoori, and Pablo Jarillo-Herrero. Correlated insulator behaviour at half-filling in magic-angle graphene superlattices. *Nature*, 556(7699):80–84, March 2018.

[19] Guorui Chen, Aaron L. Sharpe, Eli J. Fox, Ya-Hui Zhang, Shaoxin Wang, Lili Jiang, Bosai Lyu, Hongyuan Li, Kenji Watanabe, Takashi Taniguchi, Zhiwen Shi, T. Senthil, David Goldhaber-Gordon, Yuanbo Zhang, and Feng Wang. Tunable correlated chern

insulator and ferromagnetism in a moiré superlattice. *Nature*, 579(7797):56–61, March 2020.

[20] M. Serlin, C. L. Tschirhart, H. Polshyn, Y. Zhang, J. Zhu, K. Watanabe, T. Taniguchi, L. Balents, and A. F. Young. Intrinsic quantized anomalous hall effect in a moiré heterostructure. *Science*, 367(6480):900–903, February 2020.

[21] P. Blake, E. W. Hill, A. H. Castro Neto, K. S. Novoselov, D. Jiang, R. Yang, T. J. Booth, and A. K. Geim. Making graphene visible. *Applied Physics Letters*, 91(6), August 2007.

[22] L. Wang, I. Meric, P. Y. Huang, Q. Gao, Y. Gao, H. Tran, T. Taniguchi, K. Watanabe, L. M. Campos, D. A. Muller, J. Guo, P. Kim, J. Hone, K. L. Shepard, and C. R. Dean. One-dimensional electrical contact to a two-dimensional material. *Science*, 342(6158):614–617, November 2013.

[23] Régis Decker, Yang Wang, Victor W. Brar, William Regan, Hsin-Zon Tsai, Qiong Wu, William Gannett, Alex Zettl, and Michael F. Crommie. Local electronic properties of graphene on a BN substrate via scanning tunneling microscopy. *Nano Letters*, 11(6):2291–2295, May 2011.

[24] Chao-Xing Liu, Shou-Cheng Zhang, and Xiao-Liang Qi. The quantum anomalous hall effect: Theory and experiment. *Annual Review of Condensed Matter Physics*, 7(1):301–321, March 2016.

[25] Sankar Das Sarma, Michael Freedman, and Chetan Nayak. Majorana zero modes and topological quantum computation. *npj Quantum Information*, 1(1), October 2015.

[26] N. D. Mermin and H. Wagner. Absence of ferromagnetism or antiferromagnetism in one- or two-dimensional isotropic heisenberg models. *Phys. Rev. Lett.*, 17:1133–1136, Nov 1966.

[27] H. Deiseroth, K. Aleksandrov, C. Reiner, L. Kienle, and R. K. Kremer. Fe_3GeTe_2 and Ni_3GeTe_2 – two new layered transition-metal compounds: Crystal structures, HRTEM investigations, and magnetic and electrical properties. *EurJIC*, 2006(8):1561–1567, 2006.

[28] M. Alghamdi, M. Lohmann, J. Li, P. R. Jothi, Q. Shao, M. Aldosary, T. Su, B. P. T. Fokwa, and J. Shi. Highly efficient spin–orbit torque and switching of layered ferromagnet Fe_3GeTe_2. *Nano Lett.*, 19(7):4400–4405, 2019.

[29] Ping Liu, Ying Zhang, Kehan Li, Yongde Li, and Yong Pu. Recent advances in 2d van der waals magnets: Detection, modulation, and applications. *iScience*, 26(9):107584, September 2023.

[30] Cheng Gong, Lin Li, Zhenglu Li, Huiwen Ji, Alex Stern, Yang Xia, Ting Cao, Wei Bao, Chenzhe Wang, Yuan Wang, et al. Discovery of intrinsic ferromagnetism in two-dimensional van der waals crystals. *Nature*, 546(7657):265–269, 2017.

[31] Yujun Deng, Yijun Yu, Yichen Song, Jingzhao Zhang, Nai Zhou Wang, Zeyuan Sun, Yangfan Yi, Yi Zheng Wu, Shiwei Wu, Junyi Zhu, Jing Wang, Xian Hui Chen, and Yuanbo Zhang. Gate-tunable room-temperature ferromagnetism in two-dimensional Fe_3GeTe_2. *Nature*, 563(7729):94–99, October 2018.

[32] Zaiyao Fei, Bevin Huang, Paul Malinowski, Wenbo Wang, Tiancheng Song, Joshua Sanchez, Wang Yao, Di Xiao, Xiaoyang Zhu, Andrew F. May, Weida Wu, David H. Cobden, Jiun-Haw Chu, and Xiaodong Xu. Two-dimensional itinerant ferromagnetism in atomically thin Fe_3GeTe_2. *Nature Materials*, 17(9):778–782, August 2018.

[33] Samra Husremović, Catherine K. Groschner, Katherine Inzani, Isaac M. Craig, Karen C. Bustillo, Peter Ercius, Nathanael P. Kazmierczak, Jacob Syndikus, Madeline Van Winkle, Shaul Aloni, Takashi Taniguchi, Kenji Watanabe, Sinéad M. Griffin, and D. Kwabena Bediako. Hard ferromagnetism down to the thinnest limit of iron-intercalated tantalum disulfide. *Journal of the American Chemical Society*, 144(27):12167–12176, June 2022.

[34] D. A. Whitney, R. M. Fleming, and R. V. Coleman. Magnetotransport and superconductivity in dilute fe alloys of $NbSe_2$, $TaSe_2$, and TaS_2. *Phys. Rev. B*, 15:3405–3423, Apr 1977.

[35] Ben Niu, Tang Su, Brian A. Francisco, Subhajit Ghosh, Fariborz Kargar, Xiong Huang, Mark Lohmann, Junxue Li, Yadong Xu, Takashi Taniguchi, Kenji Watanabe, Di Wu, Alexander Balandin, Jing Shi, and Yong-Tao Cui. Coexistence of magnetic orders in two-dimensional magnet CrI_3. *Nano Letters*, 20(1):553–558, November 2019.

[36] David MacNeill, Justin T. Hou, Dahlia R. Klein, Pengxiang Zhang, Pablo Jarillo-Herrero, and Luqiao Liu. Gigahertz frequency antiferromagnetic resonance and strong magnon-magnon coupling in the layered crystal $CrCl_3$. *Phys. Rev. Lett.*, 123:047204, Jul 2019.

[37] Jiazhen Wu, Fucai Liu, Masato Sasase, Koichiro Ienaga, Yukiko Obata, Ryu Yukawa, Koji Horiba, Hiroshi Kumigashira, Satoshi Okuma, Takeshi Inoshita, and Hideo Hosono. Natural van der waals heterostructural single crystals with both magnetic and topological properties. *Science Advances*, 5(11), November 2019.

[38] B. Siberchicot, S. Jobic, V. Carteaux, P. Gressier, and G. Ouvrard. Band structure calculations of ferromagnetic chromium tellurides $CrSiTe_3$ and $CrGeTe_3$. *The Journal of Physical Chemistry*, 100(14):5863–5867, January 1996.

[39] Bevin Huang, Genevieve Clark, Efrén Navarro-Moratalla, Dahlia R. Klein, Ran Cheng, Kyle L. Seyler, Ding Zhong, Emma Schmidgall, Michael A. McGuire, David H. Cobden, Wang Yao, Di Xiao, Pablo Jarillo-Herrero, and Xiaodong Xu. Layer-dependent ferromagnetism in a van der waals crystal down to the monolayer limit. *Nature*, 546(7657):270–273, June 2017.

[40] C. L. Saiz, M. A. McGuire, S. R. J. Hennadige, J. van Tol, and S. R. Singamaneni. Electron spin resonance properties of CrI_3 and $CrCl_3$ single crystals. *MRS Advances*, 4(40):2169–2175, August 2019.

[41] Yujun Deng, Yijun Yu, Meng Zhu Shi, Zhongxun Guo, Zihan Xu, Jing Wang, Xian Hui Chen, and Yuanbo Zhang. Quantum anomalous hall effect in intrinsic magnetic topological insulator $MnBi_2Te_4$. *Science*, 367(6480):895–900, February 2020.

[42] T. H. Skyrme. A non-linear field theory. *Proceedings of the Royal Society of London. Series A. Mathematical and Physical Sciences*, 260(1300):127–138, February 1961.

[43] Mühlbauer Sebastian, Benedikt Binz, F Jonietz, Christian Pfleiderer, Achim Rosch, Anja Neubauer, Robert Georgii, and Peter Böni. Skyrmion lattice in a chiral magnet. *Science*, 323(5916):915–919, 2009.

[44] I. E. Dzyalosinskij. Thermodynamic theory of "weak" ferromagnetism in antiferromagnetic substances. *Sov. Phys., JETP*, 5:1259–1272, 1957.

[45] Tôru Moriya. New mechanism of anisotropic superexchange interaction. *Phys. Rev. Lett.*, 4:228–230, Mar 1960.

[46] Tôru Moriya. Anisotropic superexchange interaction and weak ferromagnetism. *Phys. Rev.*, 120:91–98, Oct 1960.

[47] M. Heide, G. Bihlmayer, and S. Blügel. Dzyaloshinskii-moriya interaction accounting for the orientation of magnetic domains in ultrathin films: Fe/W(110). *Phys. Rev. B*, 78:140403, Oct 2008.

[48] Albert Fert, Vincent Cros, and Joao Sampaio. Skyrmions on the track. *Nature nanotechnology*, 8(3):152–156, 2013.

[49] Xiangjun Xing and Yan Zhou. Skyrmion motion and partitioning of domain wall velocity driven by repulsive interactions. *Communications Physics*, 5(1), October 2022.

[50] Licong Peng, Kosuke Karube, Yasujiro Taguchi, Naoto Nagaosa, Yoshinori Tokura, and Xiuzhen Yu. Dynamic transition of current-driven single-skyrmion motion in a room-temperature chiral-lattice magnet. *Nature Communications*, 12(1), November 2021.

[51] Tae-Eon Park, Licong Peng, Jinghua Liang, Ali Hallal, Fehmi Sami Yasin, Xichao Zhang, Kyung Mee Song, Sung Jong Kim, Kwangsu Kim, Markus Weigand, Gisela Schütz, Simone Finizio, Jörg Raabe, Karin Garcia, Jing Xia, Yan Zhou, Motohiko Ezawa, Xiaoxi Liu, Joonyeon Chang, Hyun Cheol Koo, Young Duck Kim, Mairbek Chshiev, Albert Fert, Hongxin Yang, Xiuzhen Yu, and Seonghoon Woo. Néel-type skyrmions and their current-induced motion in van der waals ferromagnet-based heterostructures. *Physical Review B*, 103(10), March 2021.

[52] William Legrand, Davide Maccariello, Nicolas Reyren, Karin Garcia, Christoforos Moutafis, Constance Moreau-Luchaire, Sophie Collin, Karim Bouzehouane, Vincent Cros, and Albert Fert. Room-temperature current-induced generation and motion of sub-100 nm skyrmions. *Nano Letters*, 17(4):2703–2712, April 2017.

[53] Yubin Ji, Seungmo Yang, Hyo-Bin Ahn, Kyoung-Woong Moon, Tae-Seong Ju, Mi-Young Im, Hee-Sung Han, Jisung Lee, Seung-young Park, Changgu Lee, Kab-Jin Kim, and Chanyong Hwang. Direct observation of room-temperature magnetic skyrmion motion driven by ultra-low current density in van der waals ferromagnets. *Advanced Materials*, February 2024.

[54] Giang D. Nguyen, Jinhwan Lee, Tom Berlijn, Qiang Zou, Saban M. Hus, Jewook Park, Zheng Gai, Changgu Lee, and An-Ping Li. Visualization and manipulation of magnetic domains in the quasi-two-dimensional material Fe_3GeTe_2. *Phys. Rev. B*, 97:014425, Jan 2018.

[55] Kyoo Kim, Junho Seo, Eunwoo Lee, K.-T. Ko, B. S. Kim, Bo Gyu Jang, Jong Mok Ok, Jinwon Lee, Youn Jung Jo, Woun Kang, Ji Hoon Shim, C. Kim, Han Woong Yeom, Byung Il Min, Bohm-Jung Yang, and Jun Sung Kim. Large anomalous hall current induced by topological nodal lines in a ferromagnetic van der waals semimetal. *Nature Materials*, 17(9):794–799, July 2018.

[56] Charles W. Dunnill, Ian MacLaren, and Duncan H. Gregory. Superconducting tantalum disulfide nanotapes; growth, structure and stoichiometry. *Nanoscale*, 2(1):90–97, 2010.

[57] S. J. Hillenius, R. V. Coleman, E. R. Domb, and D. J. Sellmyer. Magnetic properties of iron-doped layer-structure dichalcogenides. *Physical Review B*, 19(9):4711–4722, May 1979.

[58] L. J. Li, W. J. Lu, X. D. Zhu, L. S. Ling, Z. Qu, and Y. P. Sun. Fe-doping–induced superconductivity in the charge-density-wave system $1T-TaS_2$. *EPL (Europhysics Letters)*, 97(6):67005, March 2012.

[59] Guolin Zheng, Maoyuan Wang, Xiangde Zhu, Cheng Tan, Jie Wang, Sultan Albarakati, Nuriyah Aloufi, Meri Algarni, Lawrence Farrar, Min Wu, Yugui Yao, Mingliang Tian, Jianhui Zhou, and Lan Wang. Tailoring dzyaloshinskii–moriya interaction in a transition metal dichalcogenide by dual-intercalation. *Nature Communications*, 12(1), June 2021.

[60] Adam Pivonka. Nanoscale imaging of phase transitions with scanning force microscopy. 2012.

[61] Naoto Nagaosa and Yoshinori Tokura. Topological properties and dynamics of magnetic skyrmions. *Nature nanotechnology*, 8(12):899–911, 2013.

[62] Arianna Casiraghi, Héctor Corte-León, Mehran Vafaee, Felipe Garcia-Sanchez, Gianfranco Durin, Massimo Pasquale, Gerhard Jakob, Mathias Kläui, and Olga Kazakova. Individual skyrmion manipulation by local magnetic field gradients. *Communications Physics*, 2(1), November 2019.

[63] B. D. Cullity and C. D. Graham. *Introduction to Magnetic Materials*. Wiley, February 2008.

[64] Akashdeep Kamra, Michael Schreier, Hans Huebl, and Sebastian T. B. Goennenwein. Theoretical model for torque differential magnetometry of single-domain magnets. *Phys. Rev. B*, 89:184406, May 2014.

[65] Y. Martin and H. K. Wickramasinghe. Magnetic imaging by '"force microscopy"' with 1000 Å resolution. *Applied Physics Letters*, 50(20):1455–1457, May 1987.

[66] D. P. Weber, D. Rüffer, A. Buchter, F. Xue, E. Russo-Averchi, R. Huber, P. Berberich, J. Arbiol, A. Fontcuberta i Morral, D. Grundler, and M. Poggio. Cantilever magnetometry of individual Ni nanotubes. *Nano Letters*, 12(12):6139–6144, November 2012.

[67] B. C. Stipe, H. J. Mamin, T. D. Stowe, T. W. Kenny, and D. Rugar. Magnetic dissipation and fluctuations in individual nanomagnets measured by ultrasensitive cantilever magnetometry. *Phys. Rev. Lett.*, 86:2874–2877, Mar 2001.

[68] Franz J. Giessibl. High-speed force sensor for force microscopy and profilometry utilizing a quartz tuning fork. *Applied Physics Letters*, 73(26):3956–3958, December 1998.

[69] Lu Chen, Fan Yu, Ziji Xiang, Tomoya Asaba, Colin Tinsman, Benjamin Lawson, Paul M. Sass, Weida Wu, B. L. Kang, Xianhui Chen, and Lu Li. Torque differential magnetometry using the qplus mode of a quartz tuning fork. *Phys. Rev. Appl.*, 9:024005, Feb 2018.

[70] Xingzhi Wang, Kezhao Du, Yu Yang Fredrik Liu, Peng Hu, Jun Zhang, Qing Zhang, Man Hon Samuel Owen, Xin Lu, Chee Kwan Gan, Pinaki Sengupta, et al. Raman spectroscopy of atomically thin two-dimensional magnetic iron phosphorus trisulfide (FePS$_3$) crystals. *2D Materials*, 3(3):031009, 2016.

[71] Jae-Ung Lee, Sungmin Lee, Ji Hoon Ryoo, Soonmin Kang, Tae Yun Kim, Pilkwang Kim, Cheol-Hwan Park, Je-Geun Park, and Hyeonsik Cheong. Ising-type magnetic ordering in atomically thin FePS$_3$. *Nano Letters*, 16(12):7433–7438, November 2016.

[72] Kenneth S. Burch, David Mandrus, and Je-Geun Park. Magnetism in two-dimensional van der waals materials. *Nature*, 563(7729):47–52, October 2018.

[73] A Avsar, H Ochoa, Francisco Guinea, B Özyilmaz, BJ Van Wees, and Ivan J Vera-Marun. Colloquium: Spintronics in graphene and other two-dimensional materials. *Reviews of Modern Physics*, 92(2):021003, 2020.

[74] Juan F. Sierra, Jaroslav Fabian, Roland K. Kawakami, Stephan Roche, and Sergio O. Valenzuela. Van der waals heterostructures for spintronics and opto-spintronics. *Nature Nanotechnology*, 16(8):856–868, July 2021.

[75] Chaolong Tang, Zhaowei Zhang, Shen Lai, Qinghai Tan, and Wei bo Gao. Magnetic proximity effect in graphene/CrBr$_3$ van der waals heterostructures. *Advanced Materials*, 32(16):1908498, March 2020.

[76] Yingying Wu, Gen Yin, Lei Pan, Alexander J Grutter, Quanjun Pan, Albert Lee, Dustin A Gilbert, Julie A Borchers, William Ratcliff, Ang Li, et al. Large exchange splitting in monolayer graphene magnetized by an antiferromagnet. *Nature Electronics*, 3(10):604–611, 2020.

[77] André Dankert and Saroj P. Dash. Electrical gate control of spin current in van der waals heterostructures at room temperature. *Nature Communications*, 8(1), July 2017.

[78] Minsoo Kim, Geon-Hyoung Park, Jongyun Lee, Jae Hyeong Lee, Jinho Park, Hyunwoo Lee, Gil-Ho Lee, and Hu-Jong Lee. Strong proximity josephson coupling in vertically stacked $NbSe_2$–graphene–$NbSe_2$ van der waals junctions. *Nano Letters*, 17(10):6125–6130, September 2017.

[79] Yingying Wu, James Jun He, Tianyi Han, Shuigang Xu, Zefei Wu, Jiangxiazi Lin, Ting Zhang, Yuheng He, and Ning Wang. Induced ising spin-orbit interaction in metallic thin films on monolayer WSe_2. *Physical Review B*, 99(12):121406, 2019.

[80] Felix Lüpke, Dacen Waters, Sergio C de la Barrera, Michael Widom, David G Mandrus, Jiaqiang Yan, Randall M Feenstra, and Benjamin M Hunt. Proximity-induced superconducting gap in the quantum spin hall edge state of monolayer WTe_2. *Nature Physics*, 16(5):526–530, 2020.

[81] Shawulienu Kezilebieke, Md Nurul Huda, Viliam Vaňo, Markus Aapro, Somesh C. Ganguli, Orlando J. Silveira, Szczepan Głodzik, Adam S. Foster, Teemu Ojanen, and Peter Liljeroth. Topological superconductivity in a van der waals heterostructure. *Nature*, 588(7838):424–428, December 2020.

[82] J.O. Island, X. Cui, C. Lewandowski, Jun Yong Khoo, E.M. Spanton, H. Zhou, D. Rhodes, J.C. Hone, T. Taniguchi, K. Watanabe, et al. Spin–orbit-driven band inversion in bilayer graphene by the van der waals proximity effect. *Nature*, 571(7763):85–89, 2019.

[83] Frances Hellman, Axel Hoffmann, Yaroslav Tserkovnyak, Geoffrey S.D. Beach, Eric E. Fullerton, Chris Leighton, Allan H. MacDonald, Daniel C. Ralph, Dario A. Arena, Hermann A. Dürr, Peter Fischer, Julie Grollier, Joseph P. Heremans, Tomas Jungwirth, Alexey V. Kimel, Bert Koopmans, Ilya N. Krivorotov, Steven J. May, Amanda K. Petford-Long, James M. Rondinelli, Nitin Samarth, Ivan K. Schuller, Andrei N. Slavin, Mark D. Stiles, Oleg Tchernyshyov, André Thiaville, and Barry L. Zink. Interface-induced phenomena in magnetism. *Reviews of Modern Physics*, 89(2), June 2017.

[84] Albert Fert, Nicolas Reyren, and Vincent Cros. Magnetic skyrmions: advances in physics and potential applications. *Nature Reviews Materials*, 2(7), June 2017.

[85] XZ Yu, Yoshinori Onose, Naoya Kanazawa, Joung Hwan Park, JH Han, Yoshio Matsui, Naoto Nagaosa, and Yoshinori Tokura. Real-space observation of a two-dimensional skyrmion crystal. *Nature*, 465(7300):901–904, 2010.

[86] F. Jonietz, S. Mühlbauer, C. Pfleiderer, A. Neubauer, W. Münzer, A. Bauer, T. Adams, R. Georgii, P. Böni, R. A. Duine, K. Everschor, M. Garst, and A. Rosch. Spin transfer torques in MnSi at ultralow current densities. *Science*, 330(6011):1648–1651, December 2010.

[87] Lingfei Wang, Qiyuan Feng, Yoonkoo Kim, Rokyeon Kim, Ki Hoon Lee, Shawn D. Pollard, Yeong Jae Shin, Haibiao Zhou, Wei Peng, Daesu Lee, Wenjie Meng, Hyunsoo Yang, Jung Hoon Han, Miyoung Kim, Qingyou Lu, and Tae Won Noh. Ferroelectrically tunable magnetic skyrmions in ultrathin oxide heterostructures. *Nature Materials*, 17(12):1087–1094, November 2018.

[88] Seonghoon Woo, Kai Litzius, Benjamin Krüger, Mi-Young Im, Lucas Caretta, Kornel Richter, Maxwell Mann, Andrea Krone, Robert M. Reeve, Markus Weigand, Parnika Agrawal, Ivan Lemesh, Mohamad-Assaad Mawass, Peter Fischer, Mathias Kläui, and Geoffrey S. D. Beach. Observation of room-temperature magnetic skyrmions and their current-driven dynamics in ultrathin metallic ferromagnets. *Nature Materials*, 15(5):501–506, February 2016.

[89] Wanjun Jiang, Pramey Upadhyaya, Wei Zhang, Guoqiang Yu, M. Benjamin Jungfleisch, Frank Y. Fradin, John E. Pearson, Yaroslav Tserkovnyak, Kang L. Wang, Olle Heinonen, Suzanne G. E. te Velthuis, and Axel Hoffmann. Blowing magnetic skyrmion bubbles. *Science*, 349(6245):283–286, July 2015.

[90] Wenjing Li, Iuliia Bykova, Shilei Zhang, Guoqiang Yu, Riccardo Tomasello, Mario Carpentieri, Yizhou Liu, Yao Guang, Joachim Gräfe, Markus Weigand, David M. Burn, Gerrit der Laan, Thorsten Hesjedal, Zhengren Yan, Jiafeng Feng, Caihua Wan, Jinwu Wei, Xiao Wang, Xiaomin Zhang, Hongjun Xu, Chenyang Guo, Hongxiang Wei, Giovanni Finocchio, Xiufeng Han, and Gisela Schütz. Anatomy of skyrmionic textures in magnetic multilayers. *Advanced Materials*, 31(14):1807683, February 2019.

[91] Roland Wiesendanger. Nanoscale magnetic skyrmions in metallic films and multilayers: a new twist for spintronics. *Nature Reviews Materials*, 1(7), June 2016.

[92] Davide Maccariello, William Legrand, Nicolas Reyren, Karin Garcia, Karim Bouzehouane, Sophie Collin, Vincent Cros, and Albert Fert. Electrical detection of single magnetic skyrmions in metallic multilayers at room temperature. *Nature Nanotechnology*, 13(3):233–237, January 2018.

[93] Dustin A. Gilbert, Brian B. Maranville, Andrew L. Balk, Brian J. Kirby, Peter Fischer, Daniel T. Pierce, John Unguris, Julie A. Borchers, and Kai Liu. Realization of ground-state artificial skyrmion lattices at room temperature. *Nature Communications*, 6(1), October 2015.

[94] Yingying Wu, Senfu Zhang, Junwei Zhang, Wei Wang, Yang Lin Zhu, Jin Hu, Gen Yin, Kin Wong, Chi Fang, Caihua Wan, Xiufeng Han, Qiming Shao, Takashi Taniguchi, Kenji Watanabe, Jiadong Zang, Zhiqiang Mao, Xixiang Zhang, and Kang L. Wang. Néel-type skyrmion in WTe_2/Fe_3GeTe_2 van der waals heterostructure. *Nature Communications*, 11(1), July 2020.

[95] Andrada-Oana Mandru, Oğuz Yıldırım, Riccardo Tomasello, Paul Heistracher, Marcos Penedo, Anna Giordano, Dieter Suess, Giovanni Finocchio, and Hans Josef Hug. Coexistence of distinct skyrmion phases observed in hybrid ferromagnetic/ferrimagnetic multilayers. *Nature Communications*, 11(1), December 2020.

[96] D. Suess, C. Vogler, F. Bruckner, P. Heistracher, and C. Abert. A repulsive skyrmion chain as a guiding track for a racetrack memory. *AIP Advances*, 8(11), November 2018.

[97] Adam S Ahmed, James Rowland, Bryan D Esser, Sarah R Dunsiger, David W McComb, Mohit Randeria, and Roland K Kawakami. Chiral bobbers and skyrmions in epitaxial FeGe/Si (111) films. *Physical Review Materials*, 2(4):041401, 2018.

[98] Jieyu Yi, Houlong Zhuang, Qiang Zou, Zhiming Wu, Guixin Cao, Siwei Tang, SA Calder, PRC Kent, David Mandrus, and Zheng Gai. Competing antiferromagnetism in a quasi-2d itinerant ferromagnet: Fe3gete2. *2D Materials*, 4(1):011005, 2016.

[99] Graham Kimbell, Paul M. Sass, Bart Woltjes, Eun Kyo Ko, Tae Won Noh, Weida Wu, and Jason W. A. Robinson. Two-channel anomalous hall effect in $SrRuO_3$. *Physical Review Materials*, 4(5), May 2020.

[100] Kajetan M Fijalkowski, Matthias Hartl, Martin Winnerlein, Pankaj Mandal, Steffen Schreyeck, Karl Brunner, Charles Gould, and Laurens W Molenkamp. Coexistence of surface and bulk ferromagnetism mimics skyrmion hall effect in a topological insulator. *Physical Review X*, 10(1):011012, 2020.

[101] A. Neubauer, C. Pfleiderer, B. Binz, A. Rosch, R. Ritz, P. G. Niklowitz, and P. Böni. Topological hall effect in a phase of MnSi. *Physical Review Letters*, 102(18), May 2009.

[102] Milan M. Milošević, Weining Man, Geev Nahal, Paul J. Steinhardt, Salvatore Torquato, Paul M. Chaikin, Timothy Amoah, Bowen Yu, Ruth Ann Mullen, and Marian Florescu. Hyperuniform disordered waveguides and devices for near infrared silicon photonics. *Scientific Reports*, 9(1), December 2019.

[103] Suk Hyun Sung, Noah Schnitzer, Lola Brown, Jiwoong Park, and Robert Hovden. Stacking, strain, and twist in 2d materials quantified by 3d electron diffraction. *Phys. Rev. Mater.*, 3:064003, Jun 2019.

[104] E. A. Marseglia. Transition metal dichalcogenides and their intercalates. *International Reviews in Physical Chemistry*, 3(2):177–216, 1983.

[105] R.H. Friend and A.D. Yoffe. Electronic properties of intercalation complexes of the transition metal dichalcogenides. *Advances in Physics*, 36(1):1–94, 1987.

[106] B. Van Laar, H.M. Rietveld, and D.J.W. Ijdo. Magnetic and crystallographic structures of Me_xNbS_2 and Me_xTaS_2. *Journal of Solid State Chemistry*, 3(2):154–160, 1971.

[107] E. Morosan, H. W. Zandbergen, Lu Li, Minhyea Lee, J. G. Checkelsky, M. Heinrich, T. Siegrist, N. P. Ong, and R. J. Cava. Sharp switching of the magnetization in $Fe_{1/4}TaS_2$. *Phys. Rev. B*, 75:104401, Mar 2007.

[108] J. G. Checkelsky, Minhyea Lee, E. Morosan, R. J. Cava, and N. P. Ong. Anomalous hall effect and magnetoresistance in the layered ferromagnet $Fe_{1/4}TaS_2$: The inelastic regime. *Phys. Rev. B*, 77:014433, Jan 2008.

[109] Chih-Wei Chen, Shalinee Chikara, Vivien S. Zapf, and E. Morosan. Correlations of crystallographic defects and anisotropy with magnetotransport properties in Fe_xTaS_2 single crystals ($0.23 \leq x \leq 0.25$). *Phys. Rev. B*, 94:054406, Aug 2016.

[110] Yoichi Horibe, Junjie Yan, Yong-Heum Cho, Xuan Luo, Sung Baek Kim, Yoon Seok Oh, Fei-Ting Huang, Toshihiro Asada, Makoto Tanimura, Dalyoung Jeong, and Sang-Wook Cheong. Color theorems, chiral domain topology, and magnetic properties of Fe_xTaS_2. *J. Am. Chem. Soc.*, 136:8368–8373, May 2014.

[111] U. K. Rößler, A. N. Bogdanov, and C. Pfleiderer. Spontaneous skyrmion ground states in magnetic metals. *Nature*, 442(7104):797–801, August 2006.

[112] Masaya Uchida, Yoshinori Onose, Yoshio Matsui, and Yoshinori Tokura. Real-space observation of helical spin order. *Science*, 311(5759):359–361, 2006.

[113] M. E. Henderson, B. Heacock, M. Bleuel, D. G. Cory, C. Heikes, M. G. Huber, J. Krzywon, O. Nahman-Levesqué, G. M. Luke, M. Pula, D. Sarenac, K. Zhernenkov, and D. A. Pushin. Three-dimensional neutron far-field tomography of a bulk skyrmion lattice. *Nature Physics*, 19(11):1617–1623, August 2023.

[114] Kai-Xuan Zhang, Hwiin Ju, Hyuncheol Kim, Jingyuan Cui, Jihoon Keum, Je-Geun Park, and Jong Seok Lee. Broken inversion symmetry in van der waals topological ferromagnetic metal iron germanium telluride. *Advanced Materials*, December 2023.

[115] Anirban Chakraborty, Abhay K. Srivastava, Ankit K. Sharma, Ajesh K. Gopi, Katayoon Mohseni, Arthur Ernst, Hakan Deniz, Binoy Krishna Hazra, Souvik Das, Paolo Sessi, Ilya Kostanovskiy, Tianping Ma, Holger L. Meyerheim, and Stuart S. P. Parkin. Magnetic skyrmions in a thickness tunable 2d ferromagnet from a defect driven dzyaloshinskii–moriya interaction. *Advanced Materials*, 34(11), February 2022.

[116] Shivam N. Kajale, Thanh Nguyen, Corson A. Chao, David C. Bono, Artittaya Boonkird, Mingda Li, and Deblina Sarkar. Current-induced switching of a van der waals ferromagnet at room temperature. *Nature Communications*, 15(1), February 2024.